1.3 Numerical Simulation of Marangoni Convection in Consideration of Free Surface Displacement (Part 5)

Hiroshi Kawamura

Science University of Tokyo

NUMERICAL SIMULATION OF MARANGONI CONVECTION IN CONSIDERATION OF FREE SURFACE DISPLACEMENT(PART 5)

Masayuki Goto*, Ichiro Ueno*, Hiroshi Kawamura* and Shinichi Yoda**

***Science University of Tokyo, 2641 Yamazaki, Noda-shi, Chiba 278-8510, Japan**

****National Space Development Agency of Japan, 2-1-1 Sengen, Tsukuba City, 305-8505, Japan**

Thermocapillary-driven convection in a half-zone liquid bridge has been extensively examined hitherto. The dynamic free-surface deformation was often observed in the experiments. Influence of the deformation upon the flow in the bridge, however, have not been understood yet. The three-dimensional thermocapillary convection has been simulated numerically with taking the dynamic deformation of the free surface into account. The shape of the liquid bridge is determined by the stress balance over the surface. The computational grid is reconstructed in accordance with the dynamic surface shape deformation. The test fluid considered is Acetone (Pr=4.4). The free surface deformation is found to be determined primarily by the pressure. A mutual relationship between the surface deformation and the pressure and other quantities is shown in the pulsating or rotating flow states. The maximum points of the deformation in the vicinity of the hot and cold disks are azimuthally twisted.

1 INTRODUCTION

The floating zone method has been proposed to produce high quality single crystal. In this method, melt is sustained between the seed and the produced single crystal rods. The crystal of a high purity is expected because this method can be operated without any contact with a vessel. This is named as the floating zone method. On the ground, a liquid bridge shape is deformed and the natural convection takes place owing to the influence of gravity. In the space environment, on the other hand, since the gravity effect becomes negligible, the single crystal with a higher quality and a larger size can be expected.

The tangential surface stress due to the thermocapillary effect over the interface of two immiscible fluids, however, can lead to a significant fluid motion called as the Marangoni convection (see e.g., Kenning 1968).

Since the mid 70's, many experiments or a number of numerical investigations on the floating zone have been carried out for a simplified model. In these studies, the floating zone was simplified to be a liquid bridge held between two coaxial circular disks, which are kept at different temperatures. This configuration, termed as a half-zone method, is aimed to simulate the upper or lower half of the floating-zone crystal growth progress with a well defined temperature difference. Marangoni convection in the phase of a small temperature difference is a 2-dimensional symmetric steady flow. The convection changes to a 3-dimensional oscillatory flow with the rotation to the direction of a circumference as a temperature difference increases. The oscillatory flow has two

patterns called as 'Pulsating flow' and 'Rotating one'. These flows appear depending upon the temperature difference. The structure in the liquid bridge is characterized further by the modal wave number m. The flow field is divided azimuthally into $2 \times m$ sectors; the alternate sector, m in total, consists of the same thermal-fluid structure.

The experiments for the thermocapillary convection have been widely conducted. Preisser et al. (1983)[2] investigated the oscillatory flow to study the effect of several parameters such as the aspect ratio and Marangoni number. Velten et al. (1991)[3] observed the periodic instability of thermocapillary convection in the cylindrical liquid bridge.

As for the numerical simulation, Kuhlmann (1993)[4] calculated the critical Reynolds number (Re_c) for the various non-dimensional numbers (Bi, Gr, Pr, A) using the linear stability analysis. Savino and Monti (1996)[5] simulated the oscillatory flow numerically and compared it with their experiments. Shevtsova et al. (1998)[6] studied the transition from two dimensional thermoconvective steady flow to a time-dependent flow considered for an axisymmetric liquid bridge of a high Prandtl number fluid (Pr = 105) with a static curved free surface.

It should be noted that most of the existing numerical simulations were conducted without considering the dynamic free surface movement. After the onset of oscillation, however, the pressure field fluctuates violently because of the unsteady flow. Therefore the free surface is expected to dynamically deform due to these fluctuation. In fact, the free surface vibration in the liquid bridge has been observed in some terrestrial experiments. Kamotani et al. (2000)[7] reported an experiment of the thermocapillary convection performed aboard the Spacelab in an open cylindrical container, and investigated the free surface movement. In addition, they analyzed the influence of surface deformation upon the critical condition in the half-zone configuration. An influence of surface vibration upon the flow field instability must be evaluated to understand the mechanism of the oscillatory flow. To the authors' knowledge, however, no numerical work has been done on the thermocapillary convection in a liquid bridge with including the dynamic deformation of the surface. The present study aims at the numerical analysis of the thermocapillary flow in the liquid bridge with the dynamic free surface deformation.

2 NOMENCLATURE

A	aspect ratio
D	diameter
g	gravity
h	heat transfer coefficient
H	height of the liquid bridge
$\mathbf{I}$	unit matrix
J	Jacobian
m	modal wave number
$\mathbf{n}$	surface-normal vector
N	normalizing dominator
P	pressure
r, θ, z	coordinates
R, R_k	position of the free surface
R_0	radius of the disk
$R_{1,2}$	main radii of curvature
$\mathbf{S}$	stress tensor
S	S-parameter
t	time
T	temperature
T_0	reference temperature
U_o	maximum veloocity
$v_{r,\theta,z}, V_{x,y}$	velocities
$\hat{v}_i$	compensated temporally velocity
$\tilde{v}_i$	temporally velocity
V	volume of the liquid bridge
$V_{\xi,\zeta,\eta}$	contravariant velocities
$\hat{V}_{\xi,\zeta,\eta}$	temporally contravariant velocities
α	contact angle
β	thermal expansion coefficient
Δ	location of the maximum surface deformation
ΔT	temperature difference between the disks
δ_S	amount of surface displacement
κ	thermal diffusivity
λ	thermal conductivity
μ	dynamic viscosity
ν	kinematic viscosity
ξ, ζ, η	coordinates in the computational domain
ρ	density
$\sigma, \sigma(T)$	surface tension
$\sigma_0(T_0)$	reference surface tension
σ_T	thermal coefficient of surface tension
τ	time in the computational domain
$\varphi, \theta_{v\theta vr}$	angle

Bi	Biot number
Bo	Bond number
Ca	Capillary number
Gr	Grashof number
Ma	Marangoni number
Pr	Prandtl number
Re	Reynolds number

3 NUMERICAL SOLUTION TECHNIQUES

3.1 Basic flow

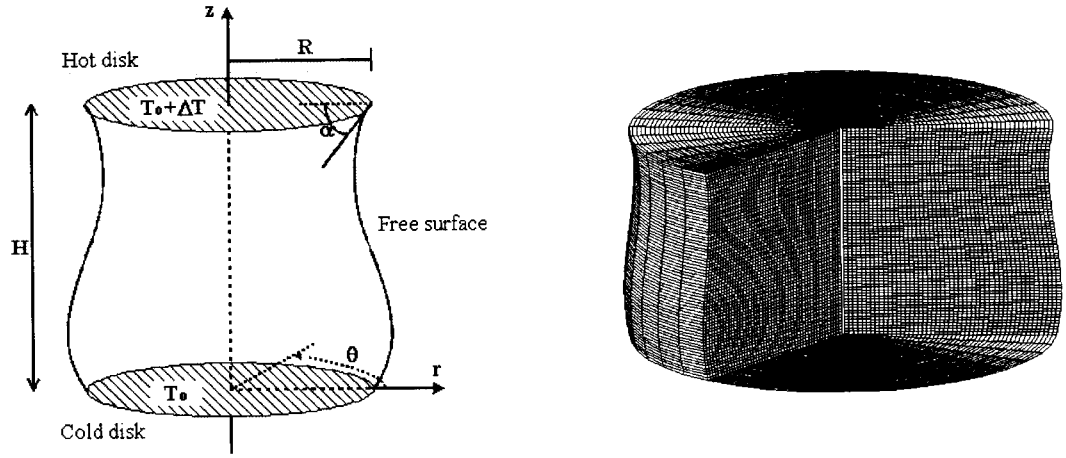

Figure 1: The configuration

The purpose of this study is to analyze the influence of the free surface deformation upon the thermocapillary flow. Therefore, a numerical method is developed to capture the temporally varying surface motion. The deformed surface is expressed using the Boundary Fitted Coordinate (B.F.C.).

The so-called half-zone model consists of a liquid bridge suspended between two rigid parallel disks of equal radii R which are located at z = 0 and H (see Fig.1). The homogeneous staggered grid is formed on the cylindrical coordinates (r, θ, z). The upper and lower disks are kept at constant temperatures T_{Hot} and T_{Cold}, respectively. The characteristic temperature is defined as ΔT=(T_{Hot}-T_{Cold}). The liquid is assumed to be an incompressible Newtonian fluid of kinematic viscosity ν and density ρ. The Boussinesq approximation is employed with a thermal expansion coefficient β. In a cylindrical coordinates system, the continuity, the Navier-Stokes and the energy equations are given by

$$\nabla \cdot \mathbf{U} = 0 \tag{1}$$

$$\frac{\partial v_i}{\partial t} + (\mathbf{U} \cdot \nabla) v_i = -\nabla P + \frac{Pr}{Ma} \nabla^2 v_i + e_z \frac{Gr}{Re^2} T \tag{2}$$

$$\frac{\partial T}{\partial t} + (\mathbf{U} \cdot \nabla) T = \frac{1}{Ma} \nabla^2 T \tag{3}$$

where $\mathbf{U}$ the velocity, $T(r, \theta, z)$ the temperature and $P(r, \theta, z)$ the pressure. The dimensionless parameters are the Reynolds, Marangoni, Prandtl and Grashof numbers defined as

$$Re = \frac{vH}{\nu}, \quad Pr = \frac{\nu}{\kappa}, \quad Ma = \frac{1}{\mu\kappa} \sigma_T \Delta T \cdot H, \quad Gr = \frac{g\beta \Delta T H^3}{\nu^2}$$

The each variable is non-dimensionalized using scales as Table 1.

Table 1: Scales used for non-dimensionalization

Variable	r, z	t	$\mathrm{v} = (v_r, v_\theta, v_z)$	p	T
Scale	H	$H\mu/\sigma_T\Delta T$	$\sigma_T\Delta T/\mu$	$\rho(\sigma_T\Delta T/\mu)^2$	ΔT

The constants σ_T, μ, κ are thermal coefficient of surface tension, dynamic viscosity and thermal diffusivity, respectively.

The shape of the liquid bridge is deformed dynamically in this calculation. Therefore, the adequate coordinate system must be employed for dynamic deformation to the calculation with use of the finite difference method. The Boundary Fitted Coordinate method is applied to the governing equations in all the directions (r, θ, z). In the previous study, the computational domain was assumed to be cube. The substantial error arises in this method of the convertion from the clynder in the pysical domain to the cube in the computational one. Thus, the present computational domain is modifyed to cylinderical coordinate. Eqs. (1)-(3) can be transformed from the physical domain to the computational domain by Jacobian matrix.

$$\begin{bmatrix} \frac{\partial}{\partial t} \\ \frac{\partial}{\partial r} \\ \frac{\partial}{\partial \theta} \\ \frac{\partial}{\partial z} \end{bmatrix} = \begin{bmatrix} 1 & \xi_t & \zeta_t & \eta_t \\ 0 & \xi_r & \zeta_r & \eta_r \\ 0 & \xi_\theta & \zeta_\theta & \eta_\theta \\ 0 & \xi_z & \zeta_z & \eta_z \end{bmatrix} \begin{bmatrix} \frac{\partial}{\partial \tau} \\ \frac{\partial}{\partial \xi} \\ \frac{\partial}{\partial \zeta} \\ \frac{\partial}{\partial \eta} \end{bmatrix} \tag{4}$$

$$\begin{bmatrix} \frac{\partial}{\partial \tau} \\ \frac{\partial}{\partial \xi} \\ \frac{\partial}{\partial \zeta} \\ \frac{\partial}{\partial \eta} \end{bmatrix} = \begin{bmatrix} 1 & r_\tau & \theta_\tau & z_\tau \\ 0 & r_\xi & \theta_\xi & z_\xi \\ 0 & r_\zeta & \theta_\zeta & z_\zeta \\ 0 & r_\eta & \theta_\eta & z_\eta \end{bmatrix} \begin{bmatrix} \frac{\partial}{\partial t} \\ \frac{\partial}{\partial r} \\ \frac{\partial}{\partial \theta} \\ \frac{\partial}{\partial z} \end{bmatrix} \tag{5}$$

Equation (5) is inversely transformed as follows,

$$\begin{bmatrix} \frac{\partial}{\partial t} \\ \frac{\partial}{\partial r} \\ \frac{1}{r}\frac{\partial}{\partial \theta} \\ \frac{\partial}{\partial z} \end{bmatrix} = \frac{1}{J} \begin{bmatrix} A_{11} & A_{12} & A_{13} & A_{14} \\ A_{21} & A_{22} & A_{23} & A_{24} \\ A_{31} & A_{32} & A_{33} & A_{34} \\ A_{41} & A_{42} & A_{43} & A_{44} \end{bmatrix} \begin{bmatrix} \frac{\partial}{\partial \tau} \\ \frac{\partial}{\partial \xi} \\ \frac{1}{\xi}\frac{\partial}{\partial \zeta} \\ \frac{\partial}{\partial \eta} \end{bmatrix}. \tag{6}$$

$$\begin{aligned}
A_{11} &= \frac{r}{\xi}(r_\xi\theta_\zeta z_\eta + r_\zeta\theta_\eta z_\xi + r_\eta\theta_\xi z_\zeta - r_\eta\theta_\zeta z_\xi - r_\zeta\theta_\xi z_\eta - r_\xi\theta_\eta z_\zeta) \\
A_{12} &= -\frac{r}{\xi}(r_\tau\theta_\zeta z_\eta + r_\zeta\theta_\eta z_\tau + r_\eta\theta_\tau z_\zeta - r_\eta\theta_\zeta z_\tau - r_\zeta\theta_\tau z_\eta - r_\tau\theta_\eta z_\zeta) \\
A_{13} &= r(r_\tau\theta_\xi z_\eta + r_\xi\theta_\eta z_\tau + r_\eta\theta_\tau z_\xi - r_\eta\theta_\xi z_\tau - r_\xi\theta_\tau z_\eta - r_\tau\theta_\eta z_\xi) \\
A_{14} &= -\frac{r}{\xi}(r_\tau\theta_\xi z_\zeta + r_\xi\theta_\zeta z_\tau + r_\zeta\theta_\tau z_\xi - r_\zeta\theta_\xi z_\tau - r_\xi\theta_\tau z_\zeta - r_\tau\theta_\zeta z\xi) \\
A_{21} &= 0, \quad A_{22} = \frac{r}{\xi}(\theta_\zeta z_\eta - \theta_\eta z_\zeta), \quad A_{23} = -r(\theta_\xi z_\eta - \theta_\eta z_\xi), \quad A_{24} = \frac{r}{\xi}(\theta_\xi z_\zeta - \theta_\zeta z_\xi) \\
A_{31} &= 0, \quad A_{32} = -\frac{1}{\xi}(r_\zeta z_\eta - r_\eta z_\zeta), \quad A_{33} = (r_\xi z_\eta - r_\eta z_\xi), \quad A_{34} = -\frac{1}{\xi}(r_\xi z_\zeta - r_\zeta z_\xi) \\
A_{41} &= 0, \quad A_{42} = \frac{r}{\xi}(r_\zeta\theta_\eta - r_\eta\theta_\zeta), \quad A_{43} = -r(r_\xi\theta_\eta - r_\eta\theta_\xi), \quad A_{44} = \frac{r}{\xi}(r_\xi\theta_\zeta - r_\zeta\theta_\xi)
\end{aligned}$$

Each component can be related from Eqs. (4) and (6) as:

$$J = \frac{r}{\xi}(r_\xi\theta_\zeta z_\eta + r_\zeta\theta_\eta z_\xi + r_\eta\theta_\xi z_\zeta - r_\eta\theta_\zeta z_\xi - r_\zeta\theta_\xi z_\eta - r_\xi\theta_\eta z_\zeta)$$

$$\xi_t = -\frac{1}{J}\frac{r}{\xi}(r_\tau\theta_\zeta z_\eta + r_\zeta\theta_\eta z_\tau + r_\eta\theta_\tau z_\zeta - r_\eta\theta_\zeta z_\tau - r_\zeta\theta_\tau z_\eta - r_\tau\theta_\eta z_\zeta)$$

$$\zeta_t = \frac{1}{J}r(r_\tau\theta_\xi z_\eta + r_\xi\theta_\eta z_\tau + r_\eta\theta_\tau z_\xi - r_\eta\theta_\xi z_\tau - r_\xi\theta_\tau z_\eta - r_\tau\theta_\eta z_\xi)$$

$$\eta_t = -\frac{1}{J}\frac{r}{\xi}(r_\tau\theta_\xi z_\zeta + r_\xi\theta_\zeta z_\tau + r_\zeta\theta_\tau z_\xi - r_\zeta\theta_\xi z_\tau - r_\xi\theta_\tau z_\zeta - r_\tau\theta_\zeta z\xi)$$

$$\xi_r = \frac{1}{J}\frac{r}{\xi}(\theta_\zeta z_\eta - \theta_\eta z_\zeta), \quad \zeta_r = -\frac{1}{J}r(\theta_\xi z_\eta - \theta_\eta z_\xi), \quad \eta_r = \frac{1}{J}\frac{r}{\xi}(\theta_{xi} z\zeta - \theta_\zeta z_\xi)$$

$$\xi_\theta = -\frac{1}{J}\frac{1}{\xi}(r_\zeta z_\eta - r_\eta z_\zeta), \quad \zeta_\theta = \frac{1}{J}(r_\xi z_\eta - r_\eta z_\xi), \quad \eta_\theta = -\frac{1}{J}\frac{1}{\xi}(r_\xi z_\zeta - r_\zeta z_\xi)$$

$$\xi_z = \frac{1}{J}\frac{r}{\xi}(r_\zeta\theta_\eta - r_\eta\theta_\zeta), \quad \zeta_z = -\frac{1}{J}r(r_\xi\theta_\eta - r_\eta\theta_\xi), \quad \eta_z = \frac{1}{J}\frac{r}{\xi}(r_\xi\theta_\zeta - r_\zeta\theta_\xi) \ .$$

The continuity, the Navier-Stokes and the energy equations (Eqs. (1)-(3)) are transformed by these rules.

[Continuity equation]

$$\frac{1}{\xi}\frac{\partial}{\partial\xi}(J\xi V_\xi) + \frac{1}{\xi}\frac{\partial}{\partial\zeta}(JV_\zeta) + \frac{\partial}{\partial\eta}(JV_\eta) = 0 \tag{7}$$

Here, V_ξ, V_ζ, V_η are defined by

$$V_\xi = \xi_r v_r + \frac{1}{r}\xi_\theta v_\theta + \xi_z v_z \ , \quad V_\zeta = \xi\zeta_r v_r + \frac{\xi}{r}\zeta_\theta v_\theta + \xi\zeta_z v_z \ , \quad V_\eta = \eta_r v_r + \frac{1}{r}\eta_\theta v_\theta + \eta_z v_z \ .$$

These velocities are called as **contravariant velocities**.

[Navier-Stokes equation]

Equation (2) is expanded as

$$\begin{aligned}
&\frac{\partial v_i}{\partial t} + \xi_t\frac{\partial v_i}{\partial\xi} + \zeta_t\frac{\partial v_i}{\partial\zeta} + \eta_t\frac{\partial v_i}{\partial\eta} \\
&+\frac{1}{J}\Big[\frac{1}{\xi}\frac{\partial}{\partial\xi}(J\xi V_\xi v_i) + \frac{1}{\xi}\frac{\partial}{\partial\zeta}(JV_\zeta v_i) + \frac{\partial}{\partial\eta}(JV_\eta v_i) + e_r\Big(-\frac{Jv_\theta^2}{r}\Big) + e_\theta\Big(\frac{Jv_r v_\theta}{r}\Big)\Big] \\
= \ & -\Big(\xi_i\frac{\partial P}{\partial\xi} + \zeta_i\frac{\partial P}{\partial\zeta} + \eta_i\frac{\partial P}{\partial\eta}\Big)e_i \\
+ \ & \frac{Pr}{Ma}\frac{1}{J}\Big[\frac{1}{\xi}\frac{\partial}{\partial\xi}(J\xi\xi_r\xi_r\frac{\partial v_i}{\partial\xi}) + \frac{1}{\xi}\frac{\partial}{\partial\xi}(J\xi\xi_r\zeta_r\frac{\partial v_i}{\partial\zeta}) + \frac{1}{\xi}\frac{\partial}{\partial\xi}(J\xi\xi_r\eta_r\frac{\partial v_i}{\partial\eta}) \\
&\quad + \frac{1}{\xi}\frac{\partial}{\partial\zeta}(J\xi\zeta_r\xi_r\frac{\partial v_i}{\partial\xi}) + \frac{\partial}{\partial\zeta}(J\xi\zeta_r\zeta_r\frac{\partial v_i}{\partial\zeta}) + \frac{\partial}{\partial\zeta}(J\xi\zeta_r\eta_r\frac{\partial v_i}{\partial\eta}) \\
&\quad + \frac{\partial}{\partial\eta}(J\eta_r\xi_r\frac{\partial v_i}{\partial\xi}) + \frac{\partial}{\partial\eta}(J\eta_r\zeta_r\frac{\partial v_i}{\partial\zeta}) + \frac{\partial}{\partial\eta}(J\eta_r\eta_r\frac{\partial v_i}{\partial\eta}) \\
&\quad + \frac{\partial}{\partial\xi}(J\frac{1}{r^2}\xi_\theta\xi_\theta\frac{\partial v_i}{\partial\xi}) + \frac{\partial}{\partial\xi}(J\frac{1}{r^2}\xi_\theta\zeta_\theta\frac{\partial v_i}{\partial\zeta}) + \frac{\partial}{\partial\xi}(J\frac{1}{r^2}\xi_\theta\eta_\theta\frac{\partial v_i}{\partial\eta})
\end{aligned}$$

$$
\begin{aligned}
&+\frac{1}{\xi}\frac{\partial}{\partial\zeta}(J\frac{\xi}{r^2}\zeta_\theta\xi_\theta\frac{\partial v_i}{\partial\xi})+\frac{1}{\xi}\frac{\partial}{\partial\zeta}(J\frac{\xi}{r^2}\zeta_\theta\zeta_\theta\frac{\partial v_i}{\partial\zeta})+\frac{1}{\xi}\frac{\partial}{\partial\zeta}(J\frac{\xi}{r^2}\zeta_\theta\eta_\theta\frac{\partial v_i}{\partial\eta})\\
&+\frac{\partial}{\partial\eta}(J\frac{1}{r^2}\eta_\theta\xi_\theta\frac{\partial v_i}{\partial\xi})+\frac{\partial}{\partial\eta}(J\frac{1}{r^2}\eta_\theta\zeta_\theta\frac{\partial v_i}{\partial\zeta})+\frac{\partial}{\partial\eta}(J\frac{1}{r^2}\eta_\theta\eta_\theta\frac{\partial v_i}{\partial\eta})\\
&+\frac{1}{\xi}\frac{\partial}{\partial\xi}(J\xi\xi_z\xi_z\frac{\partial v_i}{\partial\xi})+\frac{\partial}{\partial\xi}(J\xi\xi_z\zeta_z\frac{\partial v_i}{\partial\zeta})+\frac{\partial}{\partial\xi}(J\xi\xi_z\eta_z\frac{\partial v_i}{\partial\eta})\\
&+\frac{1}{\xi}\frac{\partial}{\partial\zeta}(J\xi\zeta_z\xi_z\frac{\partial v_i}{\partial\xi})+\frac{\partial}{\partial\zeta}(J\xi\zeta_z\zeta_z\frac{\partial v_i}{\partial\zeta})+\frac{\partial}{\partial\zeta}(J\xi\zeta_z\eta_z\frac{\partial v_i}{\partial\eta})\\
&+\frac{\partial}{\partial\eta}(J\eta_z\xi_z\frac{\partial v_i}{\partial\xi})+\frac{\partial}{\partial\eta}(J\eta_z\zeta_z\frac{\partial v_i}{\partial\zeta})+\frac{\partial}{\partial\eta}(J\eta_z\eta_z\frac{\partial v_i}{\partial\eta})\\
&+e_r\Big(-J\frac{v_r}{r^2}-J\frac{2}{r^2}\Big(\frac{1}{r}\xi_\theta\frac{\partial v_\theta}{\partial\xi}+\frac{1}{r}\zeta_\theta\frac{\partial v_\theta}{\partial\zeta}+\frac{1}{r}\eta_\theta\frac{\partial v_\theta}{\partial\eta}\Big)\Big)\\
&+e_\theta\Big(-J\frac{v_\theta}{r^2}+J\frac{2}{r^2}\Big(\frac{1}{r}\xi_\theta\frac{\partial v_r}{\partial\xi}+\frac{1}{r}\zeta_\theta\frac{\partial v_r}{\partial\zeta}+\frac{1}{r}\eta_\theta\frac{\partial v_r}{\partial\eta}\Big)\Big)\Big]\\
&+e_z\Big(\frac{Gr}{Re^2}T\Big),
\end{aligned}
\tag{8}
$$

where $v_i=(v_r,v_\theta,v_z)$.

[Energy equation]

Equation (3) is expanded as equation (9).

$$
\begin{aligned}
&\frac{\partial T}{\partial t}+\xi_t\frac{\partial T}{\partial\xi}+\zeta_t\frac{\partial T}{\partial\zeta}+\eta_t\frac{\partial T}{\partial\eta}\\
+\;&\frac{1}{J}\Big[\frac{1}{\xi}\frac{\partial}{\partial\xi}(J\xi V_\xi T)+\frac{1}{\xi}\frac{\partial}{\partial\zeta}(JV_\zeta T)+\frac{\partial}{\partial\eta}(JV_\eta T)\Big]\\
=\;&\frac{1}{Ma}\frac{1}{J}\Big[\frac{1}{\xi}\frac{\partial}{\partial\xi}(J\xi\xi_r\xi_r\frac{\partial T}{\partial\xi})+\frac{1}{\xi}\frac{\partial}{\partial\xi}(J\xi\xi_r\zeta_r\frac{\partial T}{\partial\zeta})+\frac{1}{\xi}\frac{\partial}{\partial\xi}(J\xi\xi_r\eta_r\frac{\partial T}{\partial\eta})\\
&\quad+\frac{1}{\xi}\frac{\partial}{\partial\zeta}(J\xi\zeta_r\xi_r\frac{\partial T}{\partial\xi})+\frac{\partial}{\partial\zeta}(J\xi\zeta_r\zeta_r\frac{\partial T}{\partial\zeta})+\frac{\partial}{\partial\zeta}(J\xi\zeta_r\eta_r\frac{\partial T}{\partial\eta})\\
&\quad+\frac{\partial}{\partial\eta}(J\eta_r\xi_r\frac{\partial T}{\partial\xi})+\frac{\partial}{\partial\eta}(J\eta_r\zeta_r\frac{\partial T}{\partial\zeta})+\frac{\partial}{\partial\eta}(J\eta_r\eta_r\frac{\partial T}{\partial\eta})\\
&\quad+\frac{\partial}{\partial\xi}(J\frac{1}{r^2}\xi_\theta\xi_\theta\frac{\partial T}{\partial\xi})+\frac{\partial}{\partial\xi}(J\frac{1}{r^2}\xi_\theta\zeta_\theta\frac{\partial T}{\partial\zeta})+\frac{\partial}{\partial\xi}(J\frac{1}{r^2}\xi_\theta\eta_\theta\frac{\partial T}{\partial\eta})\\
&\quad+\frac{1}{\xi}\frac{\partial}{\partial\zeta}(J\frac{\xi}{r^2}\zeta_\theta\xi_\theta\frac{\partial T}{\partial\xi})+\frac{1}{\xi}\frac{\partial}{\partial\zeta}(J\frac{\xi}{r^2}\zeta_\theta\zeta_\theta\frac{\partial T}{\partial\zeta})+\frac{1}{\xi}\frac{\partial}{\partial\zeta}(J\frac{\xi}{r^2}\zeta_\theta\eta_\theta\frac{\partial T}{\partial\eta})\\
&\quad+\frac{\partial}{\partial\eta}(J\frac{1}{r^2}\eta_\theta\xi_\theta\frac{\partial T}{\partial\xi})+\frac{\partial}{\partial\eta}(J\frac{1}{r^2}\eta_\theta\zeta_\theta\frac{\partial T}{\partial\zeta})+\frac{\partial}{\partial\eta}(J\frac{1}{r^2}\eta_\theta\eta_\theta\frac{\partial T}{\partial\eta})\\
&\quad+\frac{1}{\xi}\frac{\partial}{\partial\xi}(J\xi\xi_z\xi_z\frac{\partial T}{\partial\xi})+\frac{\partial}{\partial\xi}(J\xi\xi_z\zeta_z\frac{\partial T}{\partial\zeta})+\frac{\partial}{\partial\xi}(J\xi\xi_z\eta_z\frac{\partial T}{\partial\eta})\\
&\quad+\frac{1}{\xi}\frac{\partial}{\partial\zeta}(J\xi\zeta_z\xi_z\frac{\partial T}{\partial\xi})+\frac{\partial}{\partial\zeta}(J\xi\zeta_z\zeta_z\frac{\partial T}{\partial\zeta})+\frac{\partial}{\partial\zeta}(J\xi\zeta_z\eta_z\frac{\partial T}{\partial\eta})\\
&\quad+\frac{\partial}{\partial\eta}(J\eta_z\xi_z\frac{\partial T}{\partial\xi})+\frac{\partial}{\partial\eta}(J\eta_z\zeta_z\frac{\partial T}{\partial\zeta})+\frac{\partial}{\partial\eta}(J\eta_z\eta_z\frac{\partial T}{\partial\eta})\Big]
\end{aligned}
\tag{9}
$$

3.2 The coupling and time advancement

In this analysis, fractional step method is utilized to computate these governing equations. Euler method is adapted for time advancement. Here, the time in the computational domain is defined to be the same in the physical domain ($\tau = t$).
Equation (2) is described as

$$\frac{\partial v_i}{\partial \tau} + f_t + f_c = -\left(\xi_i \frac{\partial P}{\partial \xi} + \zeta_i \frac{\partial P}{\partial \zeta} + \eta_i \frac{\partial P}{\partial \eta}\right) e_i + f_v \,, \tag{10}$$

where f_t, f_c and f_v are the coordinate movement, convection and viscosity terms, respectively.
In fractional step method, the velocity is solved by dividing into three steps as below.

$$\tilde{v}_i = v_i^{(n)} + \Delta t \cdot \{-f_c + f_v\} \tag{11}$$

$$\hat{v}_i = \tilde{v}_i + \Delta t \cdot \{-f_t\} \tag{12}$$

$$v_i^{(n+1)} = \hat{v}_i - \Delta t \cdot \left(\xi_i \frac{\partial P^{(n+1)}}{\partial \xi} + \zeta_i \frac{\partial P^{(n+1)}}{\partial \zeta} + \eta_i \frac{\partial P^{(n+1)}}{\partial \eta}\right) e_i \tag{13}$$

Where $\tilde{v}$ means temporally velocity, and superscript (n) indicates a time step. $\hat{v}_i$ is a compensated temporally velocity in order to the movement of the computational grid. Because the free surface deforms, the computational grid must be restructured. Therefore, it is important that the influence of the computational grid movement is considered. Equation (12) is utilized to take account of the computational grid movement.
Equation (12) is considering in two dimensional coordinate for the simplicity. Jacobian matrix in two dimension can be described as

$$\begin{bmatrix} \frac{\partial}{\partial t} \\ \frac{\partial}{\partial r} \\ \frac{\partial}{\partial z} \end{bmatrix} = \begin{bmatrix} 1 & \xi_t & \eta_t \\ 0 & \xi_r & \eta_r \\ 0 & \xi_z & \eta_z \end{bmatrix} \begin{bmatrix} \frac{\partial}{\partial \tau} \\ \frac{\partial}{\partial \xi} \\ \frac{\partial}{\partial \eta} \end{bmatrix} \tag{14}$$

$$\begin{bmatrix} \frac{\partial}{\partial \tau} \\ \frac{\partial}{\partial \xi} \\ \frac{\partial}{\partial \eta} \end{bmatrix} = \begin{bmatrix} 1 & r_\tau & z_\tau \\ 0 & r_\xi & z_\xi \\ 0 & r_\eta & z_\eta \end{bmatrix} \begin{bmatrix} \frac{\partial}{\partial t} \\ \frac{\partial}{\partial r} \\ \frac{\partial}{\partial z} \end{bmatrix}. \tag{15}$$

Equation (15) is inversely transformed as follows,

$$\begin{bmatrix} \frac{\partial}{\partial t} \\ \frac{\partial}{\partial r} \\ \frac{\partial}{\partial z} \end{bmatrix} = \frac{1}{J} \begin{bmatrix} (r_\xi z_\eta - z_\xi r_\eta) & (-r_\tau z_\eta + z_\tau r_\eta) & (r_\tau z_\xi - z_\tau r_\xi) \\ 0 & z_\eta & -z_\xi \\ 0 & -r_\eta & r_\xi \end{bmatrix} \begin{bmatrix} \frac{\partial}{\partial \tau} \\ \frac{\partial}{\partial \xi} \\ \frac{\partial}{\partial \eta} \end{bmatrix}. \tag{16}$$

Then equation (12) can be expressed by equation (17).

$$\hat{v}_i = \tilde{v}_i - \Delta t \left[\xi_t \frac{\partial \tilde{v}_i}{\partial \xi} + \eta_t \frac{\partial \tilde{v}_i}{\partial \eta}\right] \tag{17}$$

From Eqs. (14) and (16), the relation of each components are given by

$$\begin{cases} J = r_\xi z_\eta - z_\xi r_\eta \\ \xi_t = \frac{1}{J}(-r_\tau z_\eta + z_\tau r_\eta), & \eta_t = \frac{1}{J}(r_\tau z_\xi - z_\tau r_\xi) \\ \xi_r = \frac{z_\eta}{J} & \eta_r = -\frac{z_\xi}{J} \\ \xi_z = -\frac{r_\eta}{J}, & \eta_z = \frac{r_\xi}{J} \end{cases} \tag{18}$$

Equation (17) is further transformed with use of equation (18).

$$\begin{aligned}\hat{v}_i &= \tilde{v}_i - \Delta t\frac{1}{J}(-r_\tau z_\eta + z_\tau r_\eta)\frac{\partial \tilde{v}_i}{\partial \xi}(r_\tau z_\xi - z_\tau r_\xi)\frac{\partial \tilde{v}_i}{\partial \eta} \\ &= \tilde{v}_i + \Delta t(\xi_r\frac{\partial \tilde{v}}{\partial \xi} + \eta_r\frac{\partial \tilde{v}}{\partial \eta})r_\tau + \Delta t(\xi_z\frac{\partial \tilde{v}}{\partial \xi} + \eta_z\frac{\partial \tilde{v}}{\partial \eta})z_\tau \end{aligned} \tag{19}$$

As the result, owing to the relations of derivation in equation (15) shown as

$$\begin{cases} \dfrac{\partial}{\partial r} = \xi_r\dfrac{\partial}{\partial \xi} + \eta_r\dfrac{\partial}{\partial \eta} \\ \dfrac{\partial}{\partial z} = \xi_z\dfrac{\partial}{\partial \xi} + \eta_z\dfrac{\partial}{\partial \eta} \end{cases} \tag{20}$$

Equation (17) is derived as equation (21).

$$\hat{v}_i = \tilde{v}_i + \Delta t\left\{\frac{\partial \tilde{v}_i}{\partial r}r_t + \frac{\partial \tilde{v}_i}{\partial z}z_t\right\} \tag{21}$$

Where $\tilde{v}_i$ is the velocity in the previous computational grid.
That is, if the computational grid moves by the amount of $\frac{\partial r}{\partial t}\Delta t$, the velocity in the restructured grid is indicated by equation (19) (see Figure. 2). Therefore, equation (17) indicates the correction of velocity with the computaional grid deformation. This approach can be adapted in the three dimension of the Navier-Stokes and the energy equations as well.

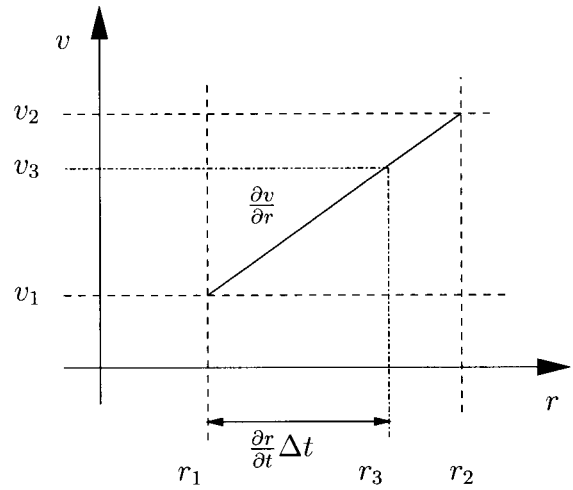

Figure 2: The relation between the velocity and the computational grid

The pressure in the equation (13) is solved by the pressure poisson equation. The pressure poisson equation is derived from the continuity equation and equation (13).
[Pressure poisson equation]

$$\nabla^2 P = \frac{\nabla \cdot v_i}{\triangle t} \tag{22}$$

Equation (22) is expanded as follows.

$$
\begin{aligned}
& \frac{\partial}{\partial\xi}(Jr\xi_r\xi_r\frac{\partial P}{\partial\xi})+\frac{\partial}{\partial\xi}(Jr\xi_r\zeta_r\frac{\partial P}{\partial\zeta})+\frac{\partial}{\partial\xi}(Jr\xi_r\eta_r\frac{\partial P}{\partial\eta}) \\
+ & \frac{\partial}{\partial\zeta}(Jr\zeta_r\xi_r\frac{\partial P}{\partial\xi})+\frac{\partial}{\partial\zeta}(Jr\zeta_r\zeta_r\frac{\partial P}{\partial\zeta})+\frac{\partial}{\partial\zeta}(Jr\zeta_r\eta_r\frac{\partial P}{\partial\eta}) \\
+ & \frac{\partial}{\partial\eta}(Jr\eta_r\xi_r\frac{\partial P}{\partial\xi})+\frac{\partial}{\partial\eta}(Jr\eta_r\zeta_r\frac{\partial P}{\partial\zeta})+\frac{\partial}{\partial\eta}(Jr\eta_r\eta_r\frac{\partial P}{\partial\eta}) \\
+ & \frac{\partial}{\partial\xi}(J\frac{1}{r}\xi_\theta\xi_\theta\frac{\partial P}{\partial\xi})+\frac{\partial}{\partial\xi}(J\frac{1}{r}\xi_\theta\zeta_\theta\frac{\partial P}{\partial\zeta})+\frac{\partial}{\partial\xi}(J\frac{1}{r}\xi_\theta\eta_\theta\frac{\partial P}{\partial\eta}) \\
+ & \frac{\partial}{\partial\zeta}(J\frac{1}{r}\zeta_\theta\xi_\theta\frac{\partial P}{\partial\xi})+\frac{\partial}{\partial\zeta}(J\frac{1}{r}\zeta_\theta\zeta_\theta\frac{\partial P}{\partial\zeta})+\frac{\partial}{\partial\zeta}(J\frac{1}{r}\zeta_\theta\eta_\theta\frac{\partial P}{\partial\eta}) \\
+ & \frac{\partial}{\partial\eta}(J\frac{1}{r}\eta_\theta\xi_\theta\frac{\partial P}{\partial\xi})+\frac{\partial}{\partial\eta}(J\frac{1}{r}\eta_\theta\zeta_\theta\frac{\partial P}{\partial\zeta})+\frac{\partial}{\partial\eta}(J\frac{1}{r}\eta_\theta\eta_\theta\frac{\partial P}{\partial\eta}) \\
+ & \frac{\partial}{\partial\xi}(Jr\xi_z\xi_z\frac{\partial P}{\partial\xi})+\frac{\partial}{\partial\xi}(Jr\xi_z\zeta_z\frac{\partial P}{\partial\zeta})+\frac{\partial}{\partial\xi}(Jr\xi_z\eta_z\frac{\partial P}{\partial\eta}) \\
+ & \frac{\partial}{\partial\zeta}(Jr\zeta_z\xi_z\frac{\partial P}{\partial\xi})+\frac{\partial}{\partial\zeta}(Jr\zeta_z\zeta_z\frac{\partial P}{\partial\zeta})+\frac{\partial}{\partial\zeta}(Jr\zeta_z\eta_z\frac{\partial P}{\partial\eta}) \\
+ & \frac{\partial}{\partial\eta}(Jr\eta_z\xi_z\frac{\partial P}{\partial\xi})+\frac{\partial}{\partial\eta}(Jr\eta_z\zeta_z\frac{\partial P}{\partial\zeta})+\frac{\partial}{\partial\eta}(Jr\eta_z\eta_z\frac{\partial P}{\partial\eta}) \\
= & \frac{1}{\triangle t}\Big[\frac{\partial}{\partial\xi}(Jr\hat{V_\xi})+\frac{\partial}{\partial\zeta}(Jr\hat{V_\zeta})+\frac{\partial}{\partial\eta}(Jr\hat{V_\eta})\Big]
\end{aligned}
\tag{23}
$$

Where $\hat{V_\xi}$,$\hat{V_\zeta}$ and $\hat{V_\eta}$ are defined by

$$
\hat{V_\xi}=\xi_r\hat{v_r}+\frac{1}{r}\xi_\theta\hat{v_\theta}+\xi_z\hat{v_z}\ ,\quad \hat{V_\zeta}=\zeta_r\hat{v_r}+\frac{1}{r}\zeta_\theta\hat{v_\theta}+\zeta_z\hat{v_z}\ ,\quad \hat{V_\eta}=\eta_r\hat{v_r}+\frac{1}{r}\eta_\theta\hat{v_\theta}+\eta_z\hat{v_z}\ ,
$$

which are called as **contravariant temporally velocities**.
To solve the pressure variation implicitly, equation (23) is calculated by successive over relaxation method (SOR method) in this analysis.

3.3 Application of Crank-Nicholson Scheme

The Crank-Nicholson Scheme is applied only the circumferential constituent of the viscous terms in the Navier-Stokes and the energy equations in order to ensure a larger stability margin. Equation (11) is discretized as

$$
\begin{aligned}
& \frac{\partial v_i}{\partial t}+(\mathbf{U}\cdot\nabla)v_i=\frac{1}{Re}\nabla^2 v_i \\
\rightarrow\quad & \frac{\partial v_i}{\partial t}+(\mathbf{U}\cdot\nabla)v_i=\frac{1}{Re}\Big\{H_i+\frac{1}{r^2}\frac{\partial^2 v_i}{\partial\theta^2}\Big\} \\
\rightarrow\quad & \frac{\widetilde{v}_i-v_i^n}{\Delta t}=\Big[-(\mathbf{U}\cdot\nabla)v_i+\frac{1}{Re}\Big\{H_i+\frac{1}{r^2}\frac{\partial^2 v_i}{\partial\theta^2}\Big\}\Big]^n \\
\rightarrow\quad & \frac{\widetilde{v}_i-v_i^n}{\Delta t}=\Big[-(\mathbf{U}\cdot\nabla)v_i+\frac{1}{Re}H_i\Big]^n+\frac{1}{Re}\frac{1}{r^2}\frac{\partial^2}{\partial\theta^2}\Big(\frac{v_i^n+\widetilde{v}_i}{2}\Big) \\
\rightarrow\quad & \Big(\frac{\Delta t}{2Re}\frac{1}{r^2}\frac{\partial^2}{\partial\theta^2}-1\Big)\widetilde{v}_i=-v_i^n-\Delta t\Big[-(\mathbf{U}\cdot\nabla)v_i+\frac{1}{Re}H_i\Big]^n-\frac{\Delta t}{2Re}\frac{1}{r^2}\frac{\partial^2 v_i^n}{\partial\theta^2}
\end{aligned}
$$

$$
\begin{aligned}
\rightarrow \quad & \frac{\Delta t}{2Re\cdot r^2\Delta\theta^2}\widetilde{v}_{i(j-1)} - \left(\frac{\Delta t}{Re\cdot r^2\Delta\theta^2}+1\right)\widetilde{v}_{i(j)} + \frac{\Delta t}{2Re\cdot r^2\Delta\theta^2}\widetilde{v}_{i(j+1)} \\
= \quad & -v_i^n - \Delta t\left[-(\mathbf{U}\cdot\nabla)v_i + \frac{1}{Re}H_i\right]^n - \frac{\Delta t}{2Re}\frac{1}{r^2}\frac{\partial^2 v_i^n}{\partial\theta^2}.
\end{aligned}
\tag{24}
$$

The Tri-Diagonal Matrix Algorithm (TDMA) is used for to solve equation (24). In the time advancement, second-order precision can be guaranteed by this method.

The energy equation is also transformed to be applied the Crank-Nicholson scheme. Equation (3) is expressed as

$$
\begin{aligned}
& \frac{\partial T}{\partial t} + (\mathbf{U}\cdot\nabla)T = \frac{1}{Ma}\nabla^2 T \\
\rightarrow \quad & \frac{\partial T}{\partial t} + (\mathbf{U}\cdot\nabla)T = \frac{1}{Ma}\left\{H_t + \frac{1}{r^2}\frac{\partial^2 T}{\partial\theta^2}\right\} \\
\rightarrow \quad & \left(\frac{\Delta t}{2Ma}\frac{1}{r^2}\frac{\partial^2}{\partial\theta^2} - 1\right)T^{n+1} = -T^n - \Delta t\left[-(\mathbf{U}\cdot\nabla)T + \frac{1}{Ma}H_t\right]^n - \frac{\Delta t}{2Ma}\frac{1}{r^2}\frac{\partial^2 T^n}{\partial\theta^2} \\
\rightarrow \quad & \frac{\Delta t}{2Ma\cdot r^2\Delta\theta^2}T_{j-1}^{n+1} - \left(\frac{\Delta t}{Ma\cdot r^2\Delta\theta^2}+1\right)T_j^{n+1} + \frac{\Delta t}{2Ma\cdot r^2\Delta\theta^2}T_{j+1}^{n+1} \\
= \quad & -T^n - \Delta t\left[-(\mathbf{U}\cdot\nabla)v_i + \frac{1}{Ma}H_t\right]^n - \frac{\Delta t}{2Ma}\frac{1}{r^2}\frac{\partial^2 T^n}{\partial\theta^2}.
\end{aligned}
\tag{25}
$$

3.4 Solution around the center axis

In the case of the numerical simulation with the 3-dimensional cylindrical coordinate system, the central axis (r = 0) becomes the singular point. This central axis problem is important for the calculations with the cylindrical coordinate system. Therefore, in the present calculation, the velocity, pressure and temperature in the central region are solved as method below. The computaitonal grid is fixed at the center.

Each radial velocities $v_r(0,j,k)$ on a central mesh and each circumferential velocity on outer one more mesh are summed from 0 to 2π.

$$
\begin{cases}
v_x(k) = \displaystyle\sum_{j=1}^{n\theta}\Big[& \{v_r(1,j,k) - v_r(1,j+n\theta,k)\}\cos\{\theta(j)-\Delta\theta/2\} \\
& - \{v_\theta(2,j,k) - v_\theta(2,j+n\theta,k)\}\sin\{\theta(j)\}\Big] \\
v_y(k) = \displaystyle\sum_{j=1}^{n\theta}\Big[& \{v_r(1,j,k) - v_r(1,j+n\theta,k)\}\sin\{\theta(j)-\Delta\theta/2\} \\
& + \{v_\theta(2,j,k) - v_\theta(2,j+n\theta,k)\}\cos\{\theta(j)\}\Big]
\end{cases}
\tag{26}
$$

where the angle in the case of v_r differs from one of v_θ owing to the difference of definition points of each velocities. The radial velocity $v_r(0,j,k)$ and the circumferential velocity $v_\theta(0,j,k)$ on the central axis are defined as the averaged velocity in each angle.

$$
\begin{cases}
v_r(0,j,k) = \dfrac{2}{n\theta}\Big[\{v_x(k)\cos\{\theta(j)-\Delta\theta/2\} + \{v_y(k)\sin\{\theta(j)-\Delta\theta/2\}\Big] \\
v_\theta(0,j,k) = \dfrac{2}{n\theta}\Big[\{-v_x(k)\sin\{\theta(j)\} + \{v_y(k)\cos\{\theta(j)\}\Big]
\end{cases}
\tag{27}
$$

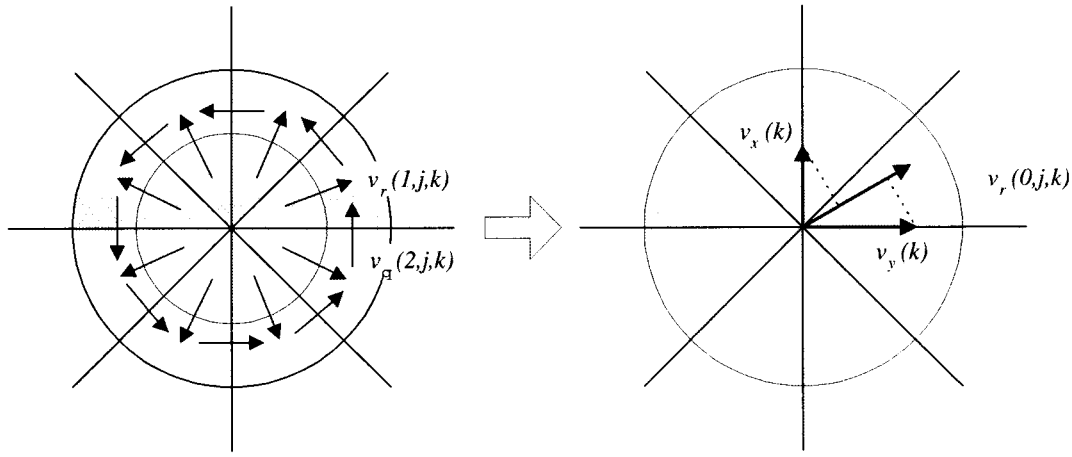

Figure 3: Calculation of velocity at center axis

The Navier-Stokes equation in the axial direction and the energy equation at the center are derived by azimuthal integration.

[Navier-Stokes equation of the liquid center (axial direction)]

$$\begin{aligned} & r\frac{\partial v_z}{\partial t} + \frac{\partial}{\partial r}(rv_r v_z) + \frac{\partial}{\partial \theta}(v_\theta v_z) + \frac{\partial}{\partial z}(rv_z^2) \\ = \; & -r\frac{\partial P}{\partial z} + \frac{Pr}{Ma}\left[\frac{\partial}{\partial r}(r\frac{\partial v_z}{\partial r}) + \frac{\partial}{\partial \theta}(\frac{1}{r}\frac{\partial v_z}{\partial \theta}) + \frac{\partial}{\partial z}(r\frac{\partial v_z}{\partial z})\right] + rT\frac{Gr}{Re^2} \end{aligned} \tag{28}$$

Equation (28) is integrated in all directions.

$$\begin{aligned} & \frac{\partial v_z}{\partial t} + \frac{\Delta\theta}{\pi\Delta r}\sum_{\theta=0}^{2\pi}(v_r v_z) + \frac{1}{\Delta z}\left[v_z^2\right]_0^{\Delta z} \\ = \; & -\frac{\partial P}{\partial z} + \frac{Pr}{Ma}\left[\frac{\Delta\theta}{\pi\Delta r}\sum_{\theta=0}^{2\pi}\frac{\partial v_z}{\partial r}\Big|_{\Delta r} + \frac{1}{\Delta z}\left[\frac{\partial v_z}{\partial z}\right]_0^{\Delta z}\right] + \frac{Gr}{Re^2}T \end{aligned} \tag{29}$$

The energy equation at the center is also derived with this treatment.
[Energy equation of the liquid center]

$$r\frac{\partial T}{\partial t} + \frac{\partial}{\partial r}(rv_r T) + \frac{\partial}{\partial \theta}(v_\theta T) + \frac{\partial}{\partial z}(rv_z T) = \frac{1}{Ma}\left[\frac{\partial}{\partial r}(r\frac{\partial T}{\partial r}) + \frac{\partial}{\partial \theta}(\frac{1}{r}\frac{\partial T}{\partial \theta}) + \frac{\partial}{\partial z}(r\frac{\partial T}{\partial z})\right] \tag{30}$$

Equation (30) is integrated in all directions.

$$\frac{\partial T}{\partial t} + \frac{\Delta\theta}{\pi\Delta r}\sum_{\theta=0}^{2\pi}(v_r T) + \frac{1}{\Delta z}\left[v_z T\right]_0^{\Delta z} = \frac{1}{Ma}\left\{\frac{\Delta\theta}{\pi\Delta r}\sum_{\theta=0}^{2\pi}\frac{\partial T}{\partial r}\Big|_{\Delta r} + \frac{1}{\Delta z}\left[\frac{\partial T}{\partial z}\right]_0^{\Delta z}\right\} \tag{31}$$

Also the pressure Poisson equation has to be solved at the liquid center axis.

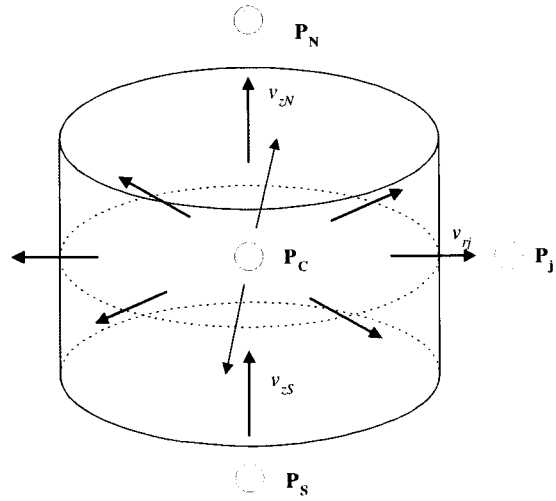

Figure 4: Center mesh

From the figure 4 the continuity equation is defined as

$$\pi\Delta r^2(v_{z_N} - v_{z_S}) + \frac{2\pi}{nj}\Delta r\Delta z\sum_{j=0}^{nj} v_{r_j} = 0. \quad (32)$$

Time advancement is described as follows.

$$\begin{cases} v_{z_N}^{(n+1)} = \tilde{v}_{z_N} - \Delta t\dfrac{P_N - P_C}{\Delta z} \\ v_{z_S}^{(n+1)} = \tilde{v}_{z_S} - \Delta t\dfrac{P_C - P_S}{\Delta z} \\ v_{r_j}^{(n+1)} = \tilde{v}_{r_j} - \Delta t\dfrac{P_j - P_C}{\Delta r + \frac{1}{2}\Delta r_j} \end{cases} \quad (33)$$

where, Δr_j is defined as $\Delta r_j = \Delta r$.

The pressure Poisson equation is derived from Eqs. (32) and (33).

$$\left[\frac{2}{\Delta z^2} + \frac{4}{3\Delta r^2}\right] P_C - \left[\frac{1}{\Delta z^2}(P_N + P_S) + \frac{1}{nj}\frac{4}{3\Delta r^2}\sum_{j=0}^{nj} P_j\right]$$
$$= \left[-\frac{1}{\Delta z}(\tilde{v}_{z_N} - \tilde{v}_{z_S}) - \frac{2}{nj\Delta r}\sum_{j=0}^{nj}\tilde{v}_{r_j}\right]\frac{1}{\Delta t} \quad (34)$$

3.5 The free surface deformation

The stress balance over the free surface must be considered to compute the free surface shape. Along the interface between two immiscible fluids (1) and (2), the forces over the surface must be balanced. If the surface is plane and the surface tension is constant, the stress balance over the surface leads

$$\mathbf{S}^{(1)} \cdot \mathbf{n} = \mathbf{S}^{(2)} \cdot \mathbf{n}, \quad (35)$$

where S is the stress tensor. The each component in the stress tensor is described as

$$S_{ij} = -P\delta_{ij} + \mu e_{ij}\,, \quad (36)$$

where $e_{i,j}$ can be expressed in the cylindrical coordinate as

$$e_{rr} = \frac{\partial v_r}{\partial r}, \quad e_{\theta\theta} = \frac{1}{r}\frac{\partial v_\theta}{\partial\theta} + \frac{v_r}{r}, \quad e_{zz} = \frac{\partial v_z}{\partial z},$$
$$e_{r\theta} = \frac{1}{2}\left\{r\frac{\partial}{\partial r}\left(\frac{v_\theta}{r}\right) + \frac{1}{r}\frac{\partial v_r}{\partial\theta}\right\}, \quad e_{\theta z} = \frac{1}{2}\left\{\frac{1}{r}\frac{\partial v_z}{\partial\theta} + \frac{\partial v_\theta}{\partial z}\right\}, \quad e_{zr} = \frac{1}{2}\left\{\frac{\partial v_r}{\partial z} + \frac{\partial v_z}{\partial r}\right\} \quad (37)$$

In addition, if the free surface has curvature and the surface tension varies along the interface, the equation of the stress balance becomes[8]

$$\mathbf{S}^{(1)} \cdot \mathbf{n} + \sigma(\nabla \cdot \mathbf{n})\mathbf{n} - (\mathbf{I} - \mathbf{nn}) \cdot \nabla\sigma = \mathbf{S}^{(2)} \cdot \mathbf{n}, \quad (38)$$

where $\mathbf{I}$ is the identity matrix, and $\mathbf{n}$ is the unit normal vector directed out of liquid (1) into the ambient fluid (2). The element $\sigma(\nabla \cdot \mathbf{n})$ in the second term is the so-called Laplace pressure. The mean curvatures of the interface,

$$\nabla \cdot \mathbf{n} = \frac{1}{R_1} + \frac{1}{R_2}, \tag{39}$$

can be expressed as the sum of the inverse principle radii of curvatures R_1 and R_2. On the other hand, the mean curvatures of the interface can be described with Cartesian coordinate system.

$$\begin{aligned} \nabla \cdot \mathbf{n} = \frac{-1}{R^3 N^3} \Bigg[& R\frac{\partial^2 R}{\partial z^2}\left\{R^2 + \left(\frac{\partial R}{\partial \theta}\right)^2\right\} \\ & + 2\frac{\partial R}{\partial z}\frac{\partial R}{\partial \theta}\left(\frac{\partial R}{\partial z}\frac{\partial R}{\partial \theta} - R\frac{\partial^2 R}{\partial z \partial \theta}\right) \\ & - \left\{1 + \left(\frac{\partial R}{\partial z}\right)^2\right\}\left\{R^2 + 2\left(\frac{\partial R}{\partial \theta}\right)^2 - R\frac{\partial^2 R}{\partial \theta^2}\right\}\Bigg]. \end{aligned} \tag{40}$$

The second additional term in equation (38) indicates the surface force acting tangentially originated from the surface tension σ. The operator $\mathbf{I} - \mathbf{nn}$ represents the orthogonal projection of a vector onto the tangent plane defined by $\mathbf{n}$. Besides the influence of the surface shape and the surface tension, the action of the gravity is taken account into the equation of the stress balance,

$$\mathbf{S}^{(1)} \cdot \mathbf{n} + \sigma(\nabla \cdot \mathbf{n})\mathbf{n} - (\mathbf{I} - \mathbf{nn}) \cdot \nabla\sigma + \rho^{(1)} g(H - z)\mathbf{n} = \mathbf{S}^{(2)} \cdot \mathbf{n} + \rho^{(2)} g(H - z)\mathbf{n} \tag{41}$$

This equation can be non-dimensionalized using the scales as Table 1.

$$\mathbf{S}^{(1)} \cdot \mathbf{n} + \left(\frac{1}{Ca} - T^*\right)(\nabla \cdot \mathbf{n})\mathbf{n} + (\mathbf{I} - \mathbf{nn}) \cdot \nabla T^* = \mathbf{S}^{(2)} - \frac{Bo}{Ca}(H - z)\mathbf{n} \tag{42}$$

where the dimensionless parameters are called the Capillary and the Bond numbers, defined as

$$Ca = \frac{\sigma_T \Delta T}{\sigma_0}, \quad Bo = \frac{(\rho^{(1)} - \rho^{(2)})gH^2}{\sigma_0} \tag{43}$$

The two tri-diagonal matrices must be considered for axial and circumferential directions, since the two directions of curvature exist in the three dimension. In addition, a constraint has to be considered to maintain the volume of the liquid bridge constant.

$$\int_0^H \int_0^{2\pi} \frac{1}{2} R^2 d\theta dz = V. \tag{44}$$

The position of the free surface R can be obtained by using Tri-Diagonal Matrix Algorithm(TDMA) in the axial and the circumferential directions derived from eqs.(40), (42) and (44) [9].

3.6 Boundary condition

To derive the boundary condition of the velocity at the free surface, the balance between the shearing stress and the surface tension must be considered. The interface both disks and fluid are assumed flat, and non-slip condition is applied for the velocity. The condition of heat transfer over the free surface is assumed to be adiabatic. Therefore, the boundary condition of velocity and

temperature can be expressed as follows.

[Velocity in the axial and horizontal directions]

$$\begin{cases} \dfrac{\partial v_s}{\partial n} = -\dfrac{\partial T}{\partial s} \\ \dfrac{1}{r}\dfrac{\partial v_r}{\partial \theta} + r\dfrac{\partial}{\partial r}(\dfrac{v_\theta}{r}) = -\dfrac{1}{r}\dfrac{\partial T}{\partial \theta} \end{cases} \tag{45}$$

[Velocity in the circumferential directions]

$$\frac{1}{r}\frac{\partial v_r}{\partial \theta} + r\frac{\partial}{\partial r}(\frac{v_\theta}{r}) = -\frac{1}{r}\frac{\partial T}{\partial \theta} \tag{46}$$

[Temperature]

$$\frac{\partial T}{\partial n} = 0 \tag{47}$$

As for the pressure, the boundary condition is derived considering the stress balance from equations (40) and (42). The pressure gradient owing to the dynamic surface deformation is applied as the condition of the pressure poisson equation (Eq. (48)) over the free surface.

$$\begin{aligned} P_{surf} = \frac{1}{Re}\Bigg[& \Bigg[\frac{\partial^2 R}{\partial z^2} - \frac{1}{R\{R^2+(\partial R/\partial\theta)^2}\Bigg[-2\frac{\partial R}{\partial z}\frac{\partial R}{\partial \theta}(\frac{\partial R}{\partial z}\frac{\partial R}{\partial \theta} - R\frac{\partial^2 R}{\partial z \partial \theta}) \\ & +\{1+(\frac{\partial R}{\partial z})^2\}\{R^2+2(\frac{\partial R}{\partial \theta})^2 - R\frac{\partial^2 R}{\partial \theta^2}\}\Bigg]\Bigg]\frac{R\{R^2+(\partial R/\partial\theta)^2\}(1/Ca-T)}{-R^3N^3} \\ & +\frac{Bo}{Ca}(H-z) \\ & +\frac{\partial v_r}{\partial r} \\ & +\frac{1}{2}\{r\frac{\partial}{\partial r}(\frac{v_\theta}{r}) + \frac{1}{r}\frac{\partial v_r}{\partial \theta}\}\frac{n_\theta}{n_r} + \frac{1}{2}\{\frac{\partial v_r}{\partial z} + \frac{\partial v_z}{\partial r}\}\frac{n_z}{n_r} \\ & +\frac{1-n_r^2}{n_r}\frac{\partial T}{\partial r} - n_\theta\frac{1}{r}\frac{\partial T}{\partial \theta} - n_z\frac{\partial T}{\partial z}\Bigg]\Bigg] \end{aligned} \tag{48}$$

4 CODE VALIDATION AND RESULTS

4.1 The initial shape of the liquid bridge without temperature difference

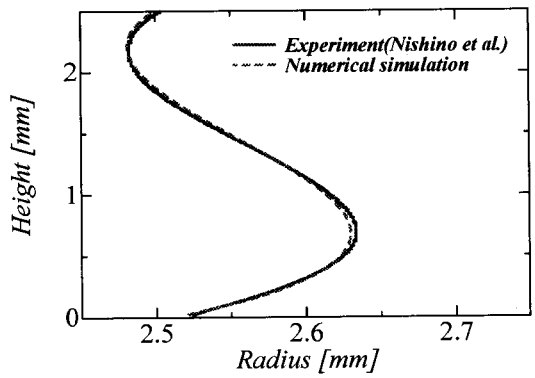

Figure 5: The shape of isothermal liquid bridge; comparison with experiment (3-dimension)

Figure 5 indicates the result of the surface shape in a case of null temperature difference. The shape is determined only by the influence of the gravity. The blue line represents an experimental result measured by Nishino[13]. The experimental conditions are: the test fluid is 5cSt of silicone oil, aspect ratio (A = Height/Diameter) of 0.5, volume ratio of 1.048. The diameter of the lower disk is slightly larger than the upper one (D_{upper} = 5mm, D_{lower} = 5.0357mm). The figure shows that the difference between experiment and numerical simulation is enough small with a maximum difference of less than 5 %. Especially, the maximum and minimum deflection points agree well with each other.

4.2 Moderate Pr number fluid

4.2.1 Static free surface deformation

Marangoni convection changes from a 2-dimensional symmetric steady flow to a 3-dimensional asymmetric oscillatory one with increasing Ma, with the circumference rotation as described in introduction. The modal wave number m is determined depending on the aspect ratio. The relation between the modal wave number and the aspect ratio is known as m×A = 1 from many experiments and numerical simulations[10]. Figure 6 shows the horizontal and the vertical temperature distribution for A = 0.5 (D = 5mm), Pr = 4.4 and Re = 2000. The steady flow (a) transits to the pulsating flow (b) on the so-called critical condition. The pulsating flow changes to the rotating flow (c) as the temperature difference increases. In the case of A = 0.5, these mode structures and the mode number of oscillation (m = 2) agree with the structures obtained by the linear stability analysis (LSA). In addition, the order of appearance of the pulsating and rotating flows also agrees well[11][12].

The simulations of liquid bridges with *statically* deformed free surface are performed. The results are first compared with LSA. Table 2 shows the conditions for the comparisons with LSA. Two cases are calculated. In Case 1, the liquid bridge is a straight cylinder with Bo = 0, while in Case 2, the surface is deformed with α = 80 where α is the contact angle between the free surface and the upper disk (Bo = 1.94, Volume ratio = 1.0). That is, in the case 1, the comparison of a liquid bridge with the statically straight surface under microgravity is performed. In the case 2, the result of simulation in a liquid bridge with the statically deformed free surface with taking the effect of gravity is validated into account. Acetone (Pr = 4.4) with A = 0.5 is assumed for both cases. Biot number Bi is defined as

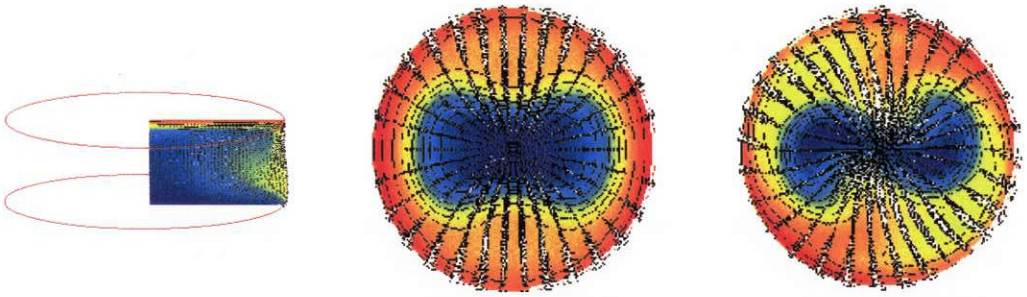

(a)Steady flow (b)Pulsating flow (c)Rotating flow

Figure 6: The flow structure of the steady and the oscillatory flows

$$Bi = \frac{hH}{\lambda} \tag{49}$$

where h and λ are the heat transfer coefficient and the thermal conductivity, respectively. The height of liquid bridge H is 2R×A with R = 2.5[mm]. The grid points of 40 × 30 × 40 (r × θ × z) are employed in these simulations.

Table 2: The parameters for comparison with linear stability analysis.

	$Case1$	$Case2$
$surface\ shape$	$cylinder$	$deformed(\alpha = 80)$
Pr	4.4	4.4
Bo	0	1.94

Fig. 7 indicates the time history of the absolute azimuthal velocity variation in case 1 at two Re numbers with the static free surface deformation under the zero gravity at the mid-height over the free surface. We calculated in various Re numbers as given in Table 3.

Table 3: Re number

Re :	1000	1500	2000

We can see that the azimuthal velocity decreases with time at Re = 1000 while it increases at Re = 2000 with a typical exponential decay or growth rate. From the growth rate of the azimuthal velocity obtained in this figure, the critical Re number can be estimated by interpolation as the point of the zero growth rate (see Fig. 8). Figure 9 indicates the azimuthal velocity variation of the case 2 for Re = 1000, 1500 and 2000.

The critical Re are compared with the result performed by LSA in Table 4. The present results of the critical Re number are obtained from figures 7 and 9. The result of case 1 is in good agreement with that of LSA. In the cases 2, the value of critical Re is a little higher than that of LSA. It is known that the critical value tends to decrease as the number of grid points increases. Therefore, it is considered that the critical Re is higher than that of LSA because the grid points are coarse. The relevant experiment with use of the Acetone is quite few because of experimental difficulty due to the high evaporation rate. Recently Kawaji[15] made a series of experiment using Acetone and obtained the critical Re of 1818 as shown in Table 4, which is much higher than the present and LSA values. The reason of the difference can be attributed to the additional cooling by the evaporation. The validity of the present program is confirmed through these examinations.

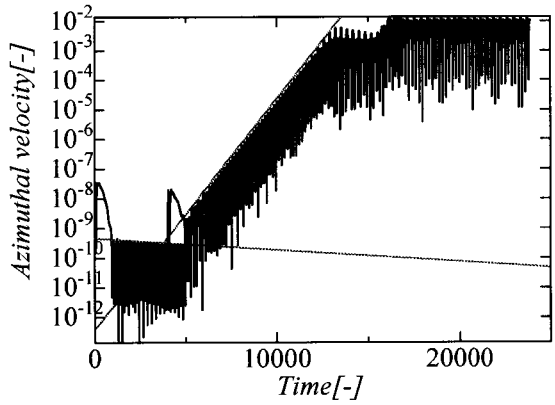

Figure 7: The azimuthal velocity variation for Re = 1000, 2000 under the zero gravity (Case 1)

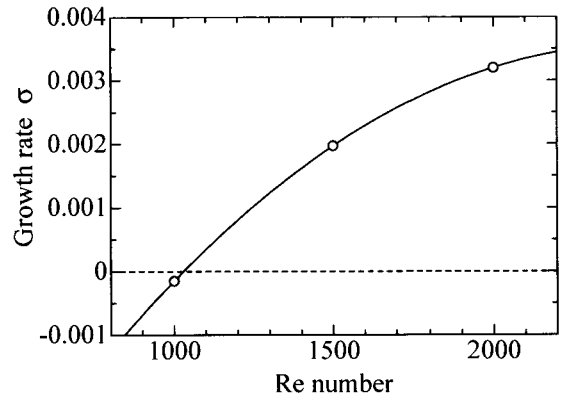

Figure 8: The growth rate of the azimuthal velocity (Case 1)

Table 4: The results of comparison with the linear stability analysis.

	*Case*1		*Case*2		
	Present	*LSA*[14]	*Present*	*LSA*[14]	*Experiment*[15]
Re_c	1050	1030	1150	1010	1818

4.2.2 Dynamic free surface deformation

Calculation are performed with the dynamic free surface deformation for Re = 1000, 1500 and 2000 under the zero gravity. The azimuthal velocity variations with dynamic free surface deformation are shown with blue lines in Figs. 10 and 11. The relation in the present calculation is Ca = 0.41×10^{-2} at Re = 2000. This volume of Ca = 0.41×10^{-2} corresponds to that of Acetone. Figure 10 indicates that the growth rate of the azimuthal velocity with static surface agrees with the one with dynamically free surface. No significant effect of free surface deformation can be found upon the critical condition.

The critical condition in the case of normal gravity with dynamic free surface deformation is also calculated. The critical Re number is slightly larger than the one with the static free surface. The effect of dynamic free surface deformation upon the critical Re is found to be quite small in the present condition.

The Ca number is one of important parameters for surface deformation. Ca number is defined as the ratio of thermal coefficient of surface tension times delta T divided by surface tension. That is, Ca = 0 means the case of dynamic non-deformable liquid bridge. In addition, the increase of ΔT results in the increase of both Re and Ca numbers. In order to further investigate the influence of surface deformation, Marangoni convection is calculated with a larger Capillary number. The orange line in the figure 12 indicates the azimuthal velocity variation with larger Ca number under the normal gravity. After all, the influence of dynamic free surface deformation upon the onset of oscillation is practically negligible in all cases calculated.

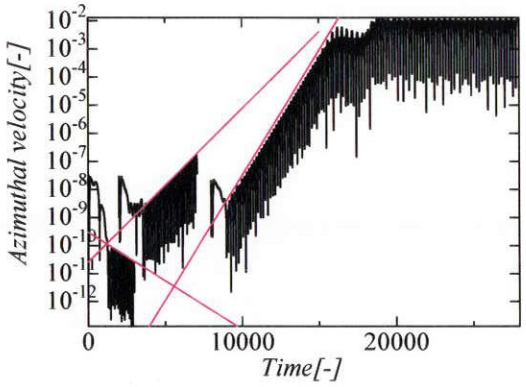

Figure 9: The azimuthal velocity variation in several Re number under the normal gravity (Case 2)

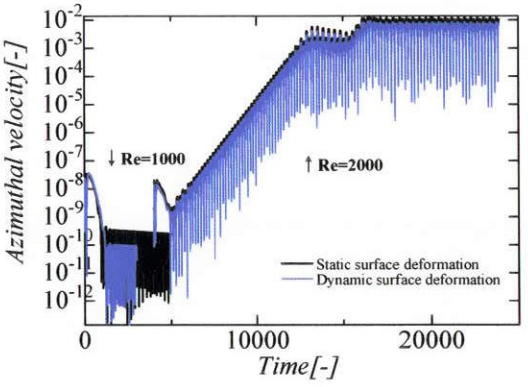

Figure 10: The azimuthal velocity variation with and without surface deformation at Re = 1000 and 2000 (g = 0 and Ca = 0.41×10^{-2} for dynamic surface deformation)

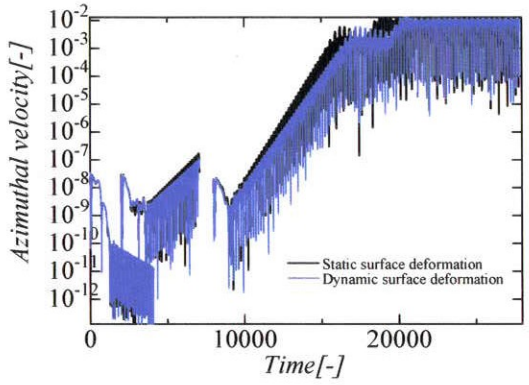

Figure 11: The azimuthal velocity variation (Re = 1000, 1500 and 2000, Ca = 0 and Ca = 0.41×10^{-2}, g = 1g)

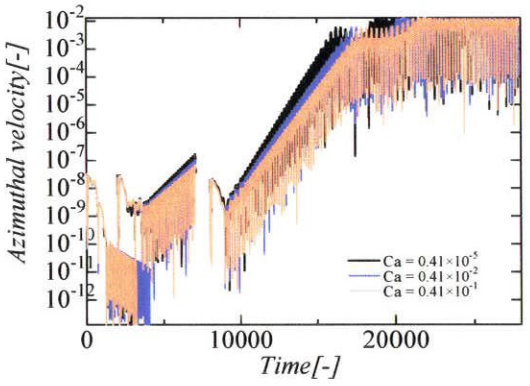

Figure 12: The azimuthal velocity variation (Re = 1000, 1500 and 2000, Ca = 0.41×10^{-1}, 0.41×10^{-2} and 0.41×10^{-5}, g = 1g

The free surface deformation with Ca = 0.41×10^{-1}, 0.41×10^{-2} and 4.1×10^{-6} is obtained at the position of 1/4H, 1/2H and 3/4H. The time history of the free surface deformation at the mid-height is shown in Fig. 13 for Ca = 0.041, 0.0041 and 4.1×10^{-6} and Re = 2,000 under the normal gravity. The free surface starts oscillating at about 8000 of the nondimentional time t. The amplitude once tends to be approximately constant and then becomes larger again at t = 13000 (see Fig. 13(a),(b)). The flow structure changes from the pulsating flow to the rotating one at that time. The amplitude at 3/4H, however, is unchanged. In the rotating flow state, the amplitude of surface deformation at the mid-height is about $0.1\mu m$ for D = 5mm. Kawaji[15] found in his experiment that the maximum dynamic deformation was an order of $0.1\mu m$ or less. So, the present results agree well with his finding.

Figure 14 shows the Ca number versus the amplitude of the surface oscillation. The amplitude increases in proportion to Ca number in the present range, which is in accordance with the tendency indicated by Kuhlmann[16] in the work.

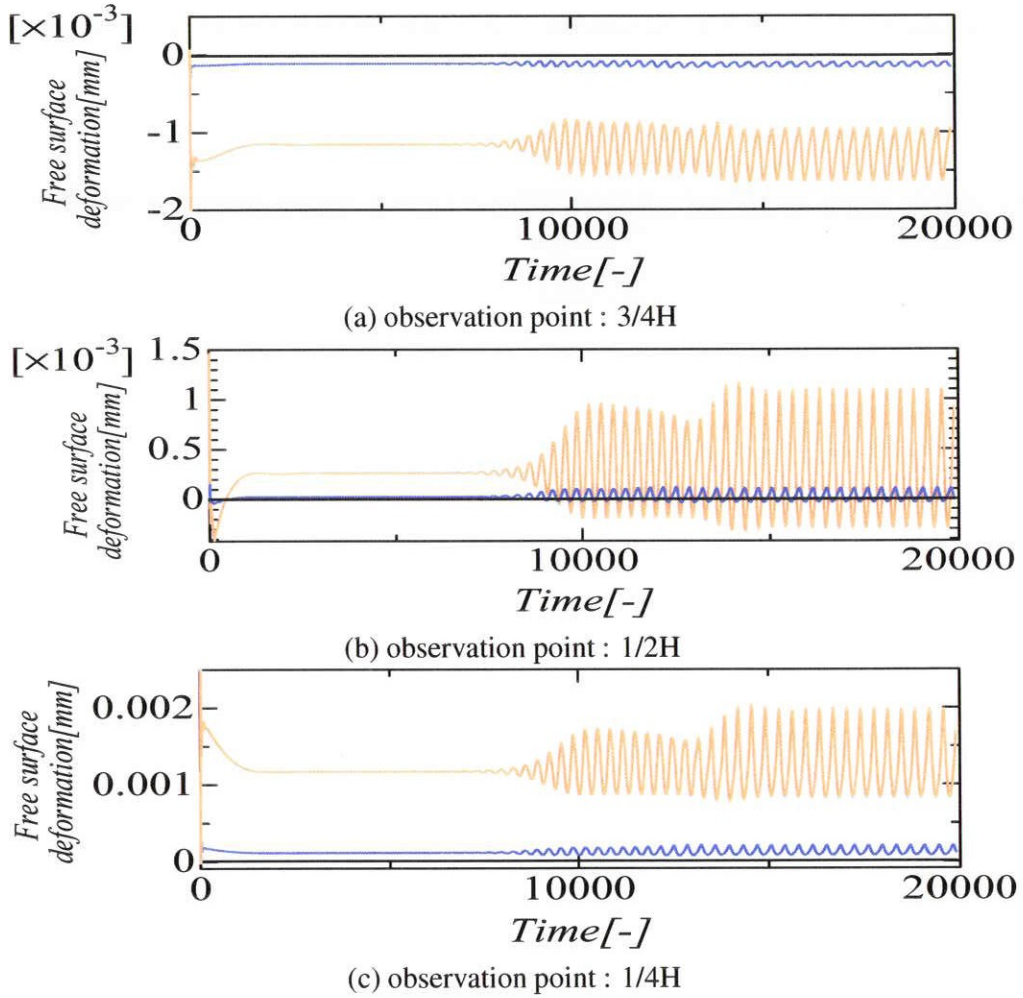

Figure 13: The time history of the surface deformation observed at 1/4H, 1/2H and 3/4H

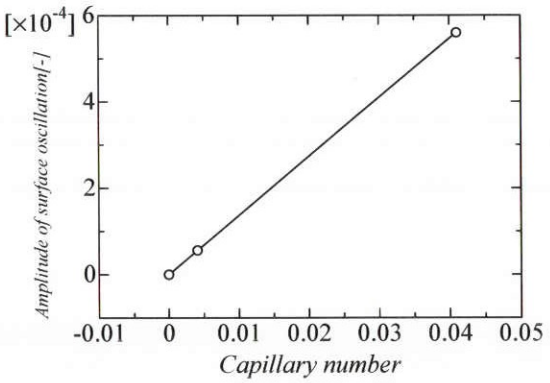

Figure 14: The amplitude of surface deformation after the onset of the oscillation for Re = 2000, Ca = 0.41×10^{-1}, 0.41×10^{-2}, 0.41×10^{-5}, g = 1g

Figure 15 indicates the temperature over the free surface at each Ca number. The temperature oscillation starts behind time with the larger Ca number. Unlike the case of the free surface, the amount of the amplitude of the temperature vibration is not different between the pulsating and the rotating flow states. The temperature at the upper part is oscillating somewhat larger than the lower one.

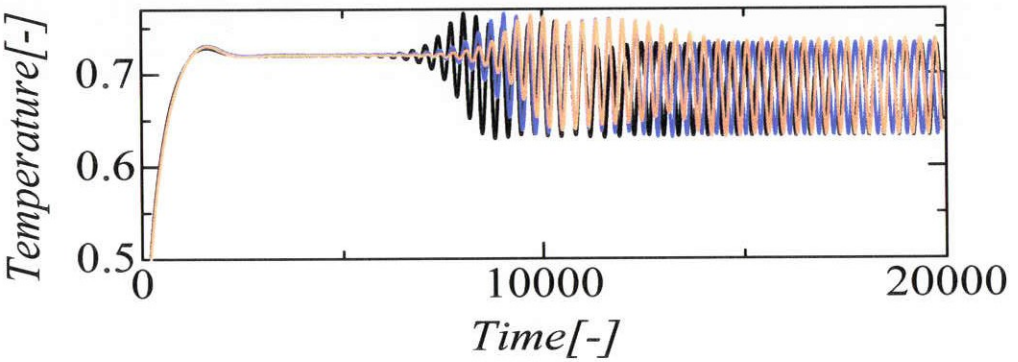

(a) observation point : 3/4H

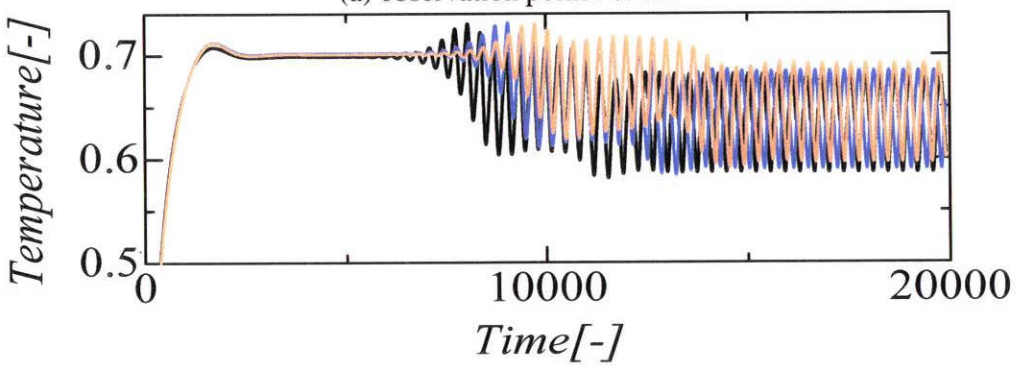

(b) observation point : 1/2H

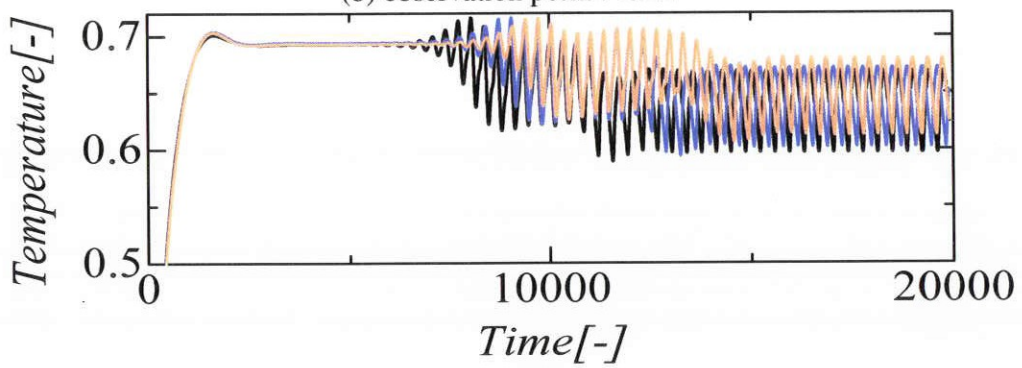

(c) observation point : 1/4H

Figure 15: The time history of the temperature observed at 1/4H, 1/2H and 3/4H

The amplitude of the axial velocity is different in accordance with the flow structure. The amplitude in the rotating flow state at the mid-height is smaller than the one in the pulsating flow state (see Figure 16(b)) The other positions show the opposite phenomena (see Figure 16(a) and (c)). The axial velocity increases or decreases at the onset of the rotating flow depend on the direction of the radial velocity over the free surface. The axial velocity with larger Ca number is larger at the upper region. The effect of Ca number upon the amplitude is quite small.

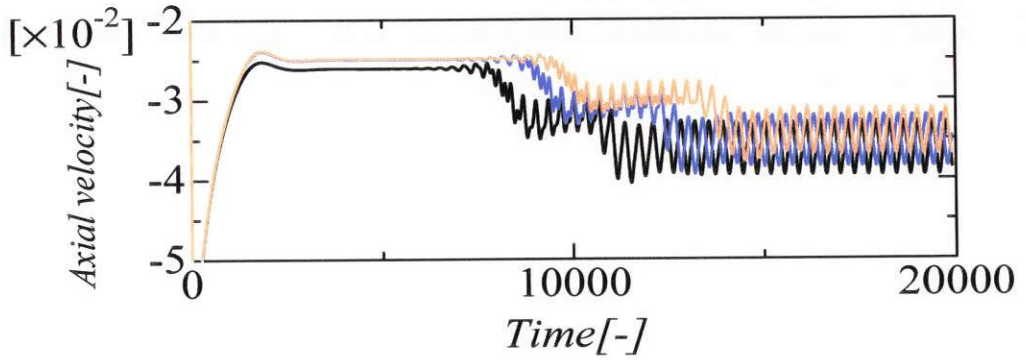

(a) observation point : 3/4H

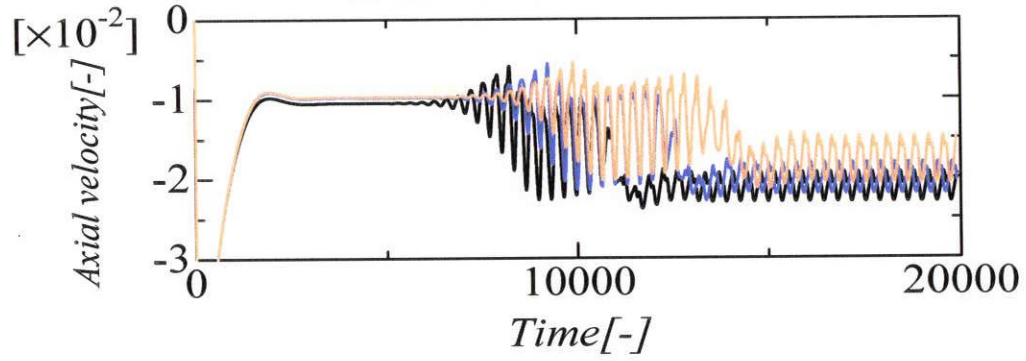

(b) observation point : 1/2H

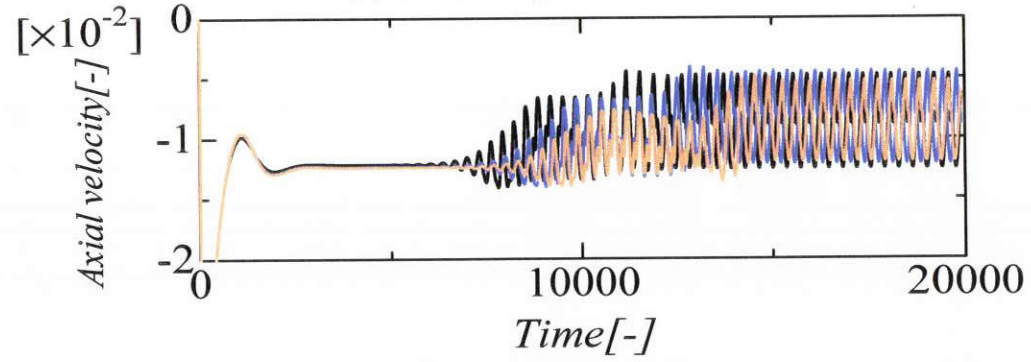

(c) observation point : 1/4H

Figure 16: The time history of the axial velocity observed at 1/4H, 1/2H and 3/4H

The mutual relationship among the free surface deformation, the temperature and pressure variations is investigated. Figure 17 shows the fluctuations of these quantities in the liquid bridge in the pulsating (a) and rotating(b) flow states. The fluctuation of the free surface displacement from the initial position is magnified with 5000. The purple, blue, red and yellow express the high temperature, the low temperature, the high pressure and the low pressure, respectively. The low or high temperature regions correspond the low or high pressure regions, respectively at the vicinity of hot disk. The axial symmetric surface deformation is observed in the pulsating flow state (see Fig.17(a)), while the free surface is deformed asymmetry due to azimuthal rotation in the rotating flow state (see Fig.17(b)). That is, the liquid bridge is twisted, and rotates holding this shape.

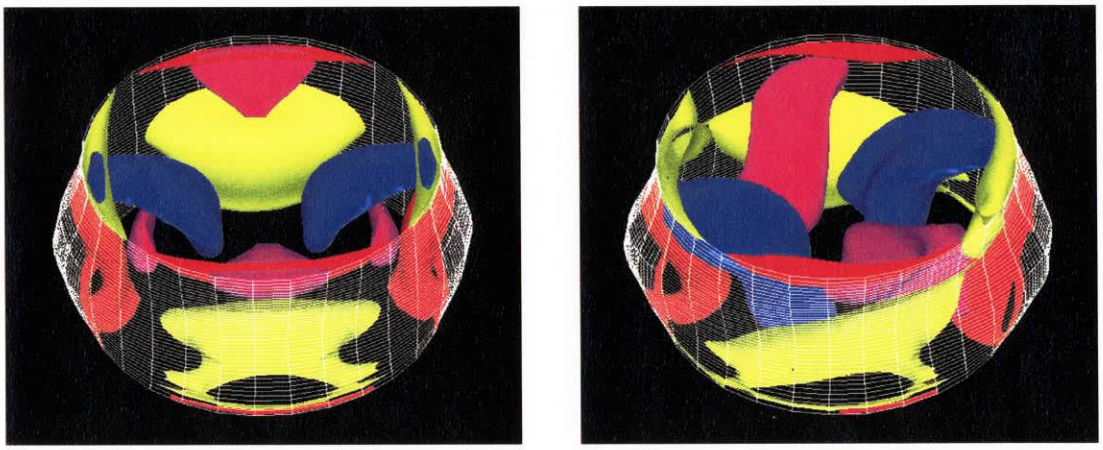

(a) (b)

Figure 17: Fluctuations of the temperature, pressure and surface deformation in the pulsating(a) and rotating(b) flow states

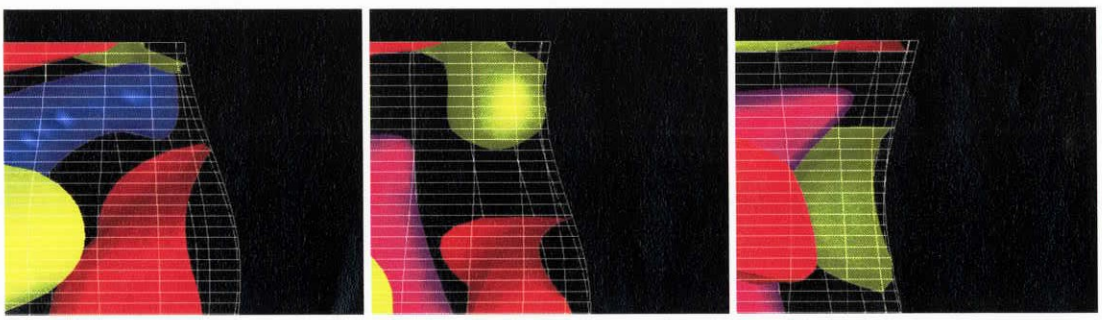

(a) (b) (c)

Figure 18: The pressure, temperature fluctuations and the free surface deformation near the upper disk

Figure 18(a) indicates the instance at which the low temperature fluid arrives at the free surface of the hot corner. The fluid over the free surface is then accelerated downward by the Marangoni force. As the result, the low pressure region appears near the upper disk owing to the Bernoulli's theorem (see Figure 18(a)). As the liquid near the upper disk flows downward, the low pressure region moves down. Consequently the surface becomes concave due to the low pressure in accordance with the stress balance (see Figure 18(c)). Phase lags among the surface deformation,

the temperature and velocity can be expected, since the dynamic free surface deformation is not directly caused by the low temperature region.

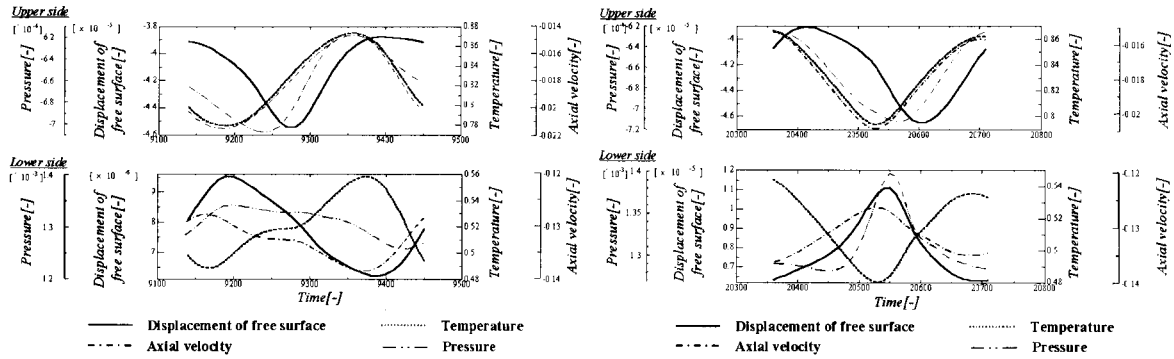

(a) (b)

Figure 19: Relationship between the surface deformation, pressure, temperature and velocity in the pulsating(a) and the rotating flow state(b)

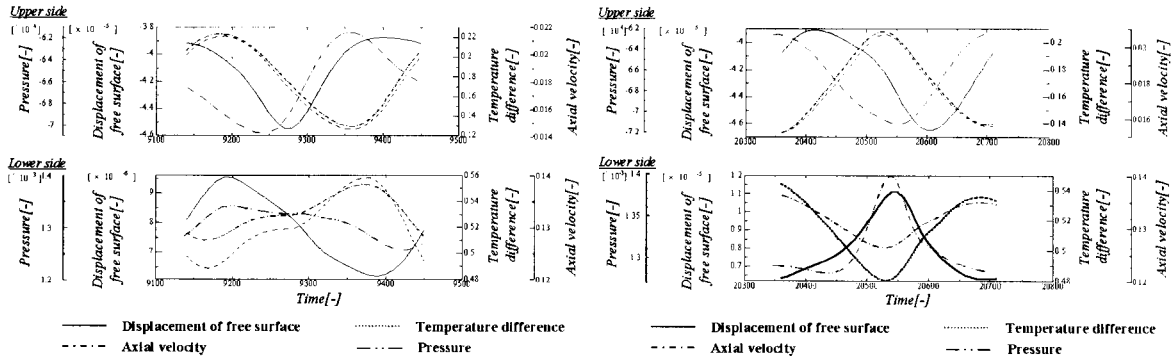

(a) (b)

Figure 20: Relationship between the surface deformation, pressure, temperature difference and absolute velocity in the pulsating(a) and the rotating flow state(b)

Figure 19 shows the phase correlation between the dynamic free surface deformation and the other quantities in the oscillatory flow state. These oscillations are observed at the points at 1/10H from either the upper or lower disks. These figures show the one cycle of oscillation in the (a)pulsating and (b)rotating flow states. The figure indicates that the phase lag of about $\pi/2$ between the temperature and the surface deformation near the upper disk in the both cases. The surface velocity oscillates in phase with the temperature. The relationship among these phases can be explained by considering that the surface deformation is not affected directly by change of the surface temperature and velocity. As for the region near the lower disk, on the other hand, the phase difference of π appears between the temperature and the velocity variation. The velocity, however, becomes maximum, when a loocal temperature difference from the temperature of lower disk is the largest. Thus, the same phase lag as the case of the upper region is brought by considering relation between a temperature difference and absolute velocity (see Figure 20). In addition,

the phase of displacement of the free surface is shifted π or slightly larger than π compared with that of the surface velocity and temperature.

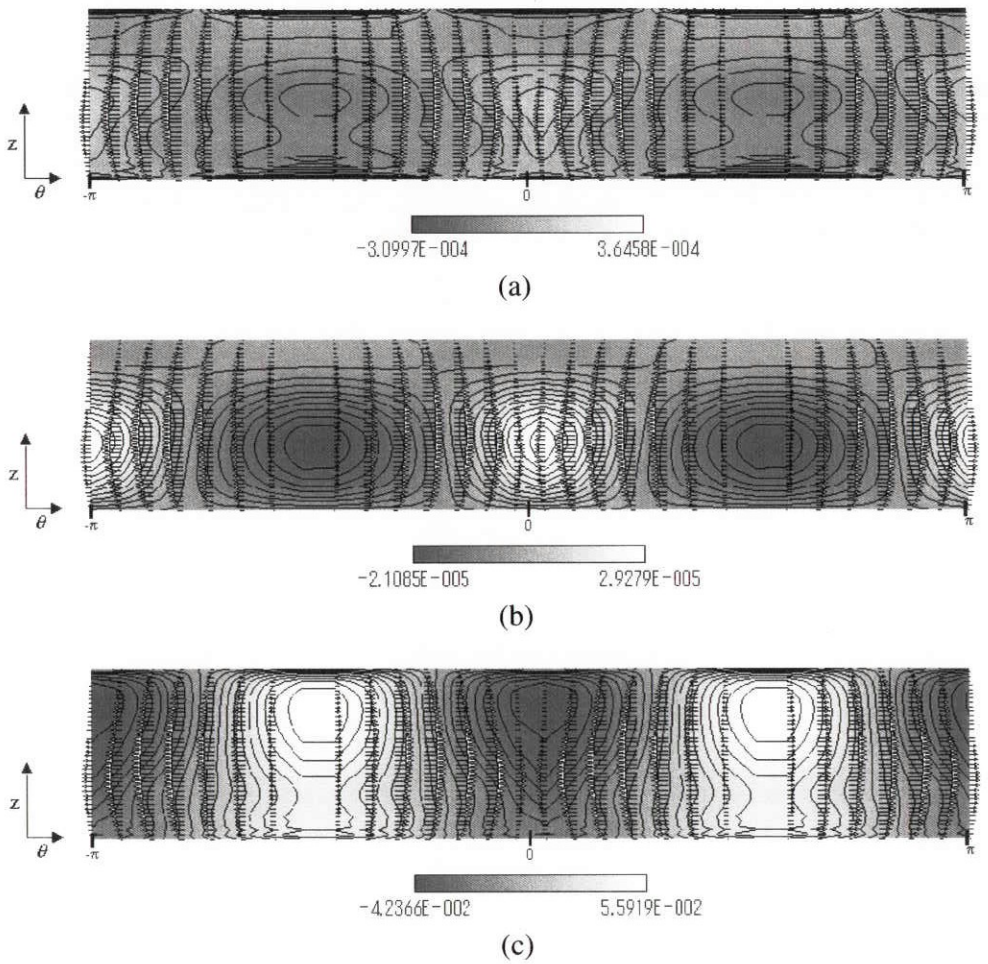

Figure 21: The fluctuations of the (a)pressure, (b)surface deformation and (c)temperature and the azimuthal velocity in the pulsating flow state on the $\theta - z$ plane

Figure 21(a) indicates the fluctuation of the pressure distribution and the azimuthal velocity on the free surface shown in the $\theta - z$ plane in the pulsating flow state. High pressure region emarges where the fluid is gathered over the surface. That is, since the pressure mainly determines the surface deformation, the high-pressure part is in accordance with the convex surface (see Fig.21(b)).

Figures 21(c) shows the temperature distribution and the azimuthal velocity on the whole free surface. Figure 21(c) indicates that the azimutha velocity vectors are directed towards the coldest temperature zone. The resultant impingement causes the high pressure region (see Fig.21(a)) and thus results in a concaved surface (Fig.21(b)). In the case of the upper region, the free surface is concaved at $\theta = 0$ point where the temperature becomes low, since the temperature difference becomes large (see Figs.21(b) and 21(c)). Therefore, the axial temperature difference govern the surface deformation near the upper disk, while the azimuthal one influences to the surface deformation near the lower disk.

As for the case of the rotating flow state, the bulging or denting regions incline notably as against an axis (see Fig.22(b)). The temperature, however, is distributed as approximately same as the case of the pulsating flow state (see Fig.22(c)). The present relation between the surface deformation and temperature agrees well with that of linear stability analysis which is obtained by Kuhlmann et al.[16]. On almost all the domains on the free surface, the free surface bulges at the low temperature area by the influence of azimuthal Marangoni force. At the vicinity of the hot disk, the phase lag between the dynamic surface deformation and temperature is shifted by the influence of the axial one in the both states.

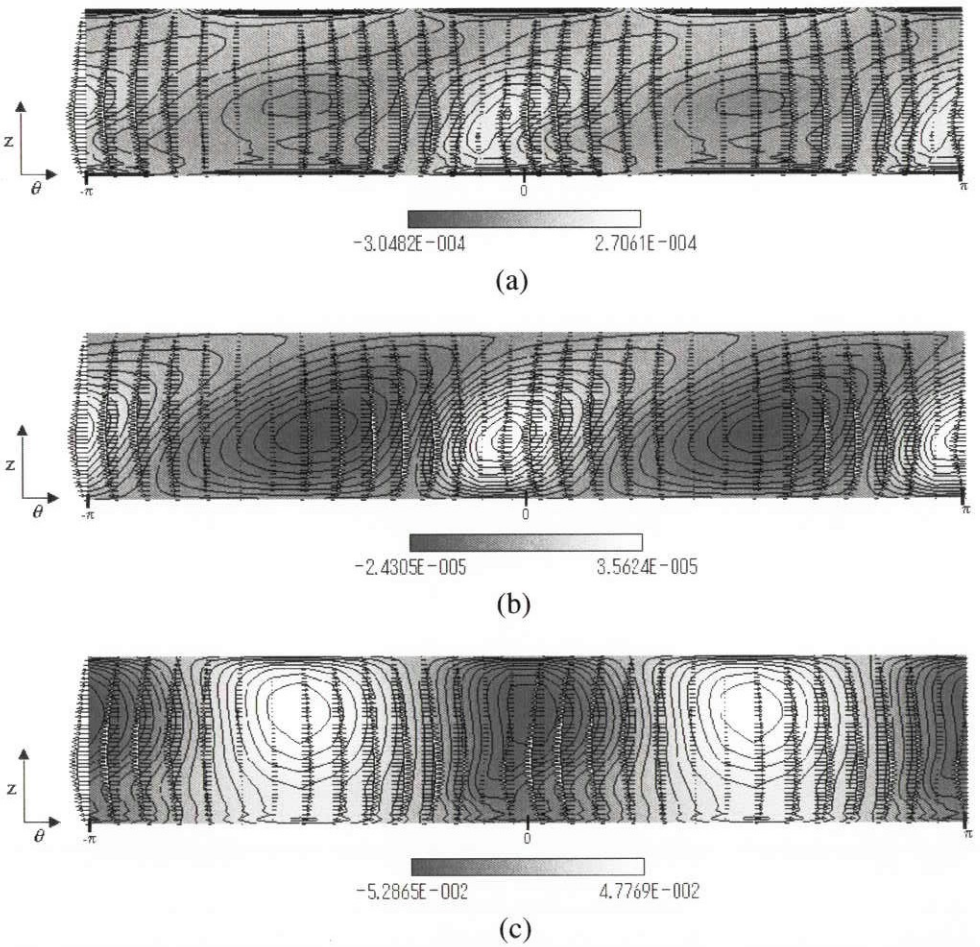

Figure 22: The fluctuations of the (a)pressure, (b)surface deformation and (c)temperature and the azimuthal velocity in the rotating flow state on the $\theta - z$ plane

Figure 23(a) indicates the shape of the liquid bridge section corresponding with figure 21. The phase of surface deformation is shifted only near the upper disk. Figure 23(b) shows the shape of liquid bridge in the rotating flow state. Although the relation of deformation of each height does not change, the center axis of each shape is incongruents each other.

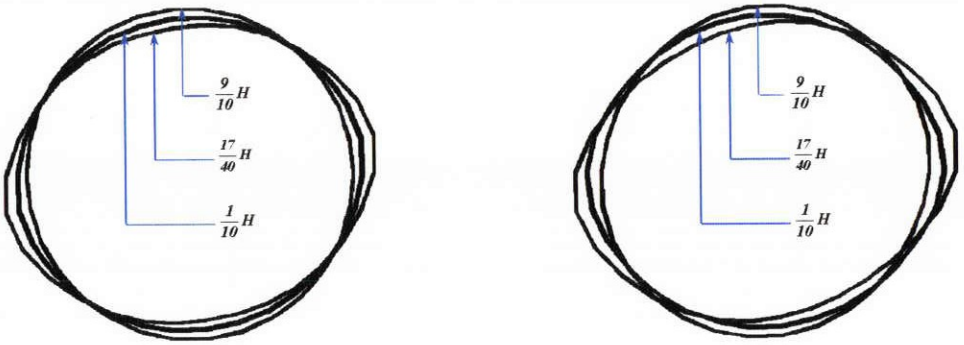

(a) (b)

Figure 23: Top view of the shape of the liquid bridge section at 1/10H, 17/40H and 9/10H in the pulsating(a) and rotating(b) flow states

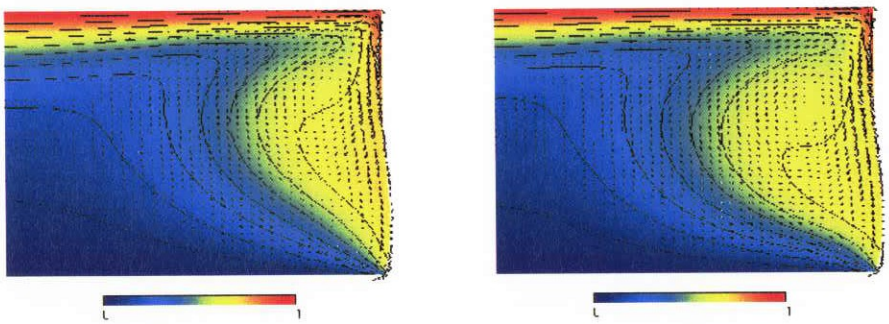

(a) (b)

Figure 24: The flow fields in the cases of the dynamic (a) and the static (b) surface deformation

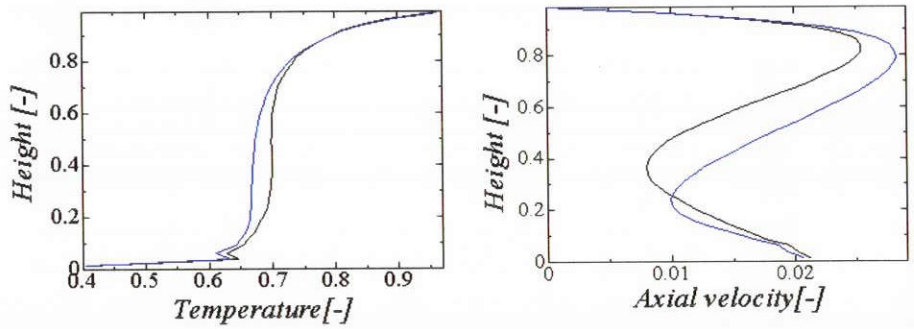

(a) (b)

Figure 25: The vertical variations of the temperature (a) and axial velocity (b) (blue line: static surface deformation, black line: dynamic surface deformation)

Fig 24 compares the flow field with dynamic and fixed surface deformations. Fig 25 indicates the temperature and the axial velocity distribution along the free surface. Figure 24 shows that in the case of dynamic surface deformation, a smaller vortex is formed, and its vortical center locates at a higher position. The velocity is more decelerated due to the enhanced viscosity effect of the smaller vortex. In addition, the surface temperature is higher, because a return flow temperature remains higher according to the smaller vortex.

The S-parameter is reported as an important nondimensional parameter to express the critical condition by Kamotani et al.[17]. The S-parameter is defined as

$$S = \frac{\sigma_T \Delta T}{\sigma} \frac{1}{Pr} Ma^{\frac{3}{14}} \tag{50}$$

The convection becomes oscillatory when the S-parameter is larger than about 0.01 in a limited range of A ($0.5 \leq A \leq 1.5$) and Pr ($7 \leq Pr \leq 81$). It is noted that the S-parameter with the critical Ma number is constant in this range. Figure 26 shows representative exisiting data for the onset of oscillations are correlated in terms of the S-parameter and Ma. The present and the compared data above are plotted on figure 26. All of the numerical and the analytical results seem not to be significant for the Kamotani's theory. Also the experimental result is smaller than 0.01. In

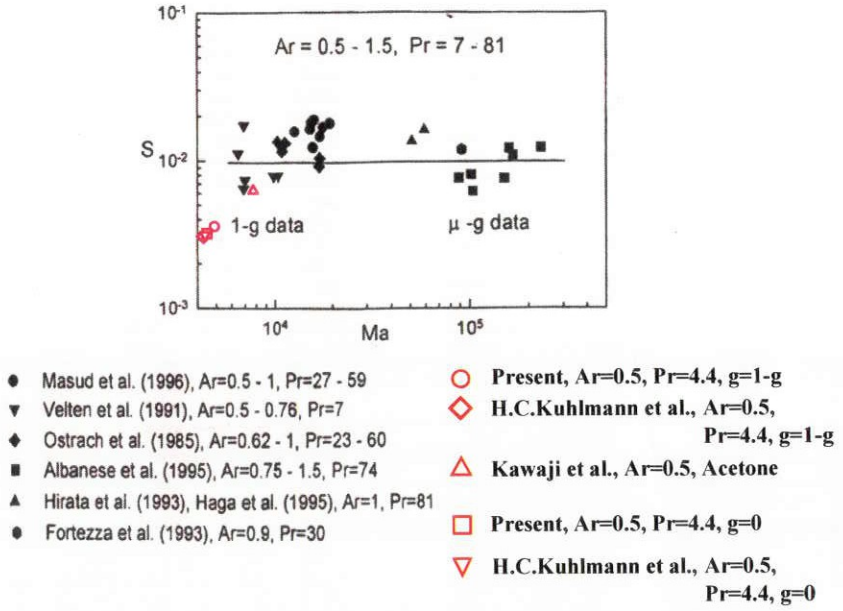

Figure 26: S-parameter

order to investigate the effect of free surface deformation upon the onset of the oscillation further, the location of the maximum surface deformation, the maximum surface velocity and the amount of the free surface displacement are compared with values obtained by Kamotani's theory. Each values are derived from equations (51), (52) and (53) (see Kamotani et al., 1998[17]).

[The location of the maximum surface deformation]

$$\Delta = Ma^{-\frac{1}{2}}L \tag{51}$$

[The maximum surface velocity]

$$U_o = \frac{\sigma_T \Delta T}{\mu} Ma^{-\frac{1}{7}} \tag{52}$$

[The amount of the free surface displacement]

$$\delta_S = \left(\frac{\sigma_T \Delta T}{\sigma}\frac{1}{Pr}\right) Ma^{-\frac{11}{28}}L \tag{53}$$

where L is the characteristic length used by Kamotani et al. According to their theory, the position of the maximum surface deformation agrees that of the maximum surface velocity. In the present result, however, these positioons differ each other. Thus, Thus, the values in the present result are observed at the points of the maximum velocity and the maximum surface deformation (see Table 5). In the present calculation, table 5 shows the maximum velocity and surface deformation is smaller, and Δ is further from the upper disk than Kamotani's results. These data are obtained with Pr = 4.4. Although the condition is slightly deviated from the defined range, it is proved that this theory is inapplicable to the moderate Pr number fluid.

Table 5: The comparison of each values derived from S-parameter

	Kamotani et al.[17]	Present (at U_{max})	Present (at δ_S)
$\Delta[mm]$	3.758×10^{-2}	2.813×10^{-1}	4.063×10^{-1}
$U_o[m/s]$	4.914×10^{-2}	6.231×10^{-3}	6.096×10^{-3}
$\delta_S[mm]$	2.015×10^{-3}	6.553×10^{-5}	6.943×10^{-5}

4.3 High Pr number fluid

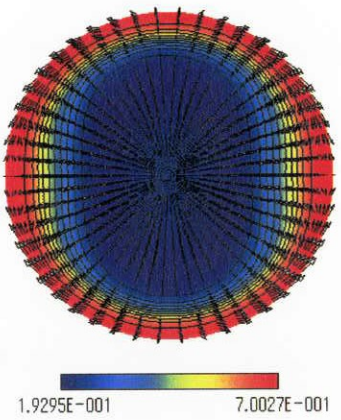

Figure 27: Temperature distribution with 2cSt in the pulsating flow state (Ma = 50000, Pr = 28, g = 1g)

In a experiment under the micro gravity, the high Pr number fluid is used as the test fluid to generate a single crystal. Hence the simulation of thermocapillary flow with high Pr number fluid is absolutely essential for crystal growth.

Figure 27 indicates the temperature distribution in the pulsating flow state at z = 1/2H. We can see that the modal structure with wave number 2 is clearly observed. Marangoni number of 50000 is employed in this calculation, and it is appreciably higher than the critical Ma number in the experiment. Therefore the convection is expected to evolve to the rotating flow. Calculation with high Pr number fluid, however, is difficult since it requires a fine mesh and a shorter time step.

Figures 28 and 29 indicate the absolute azimuthal velocity and free surface deformation, respectively. The azumuthal velocity increases with typical exponential growth rate as in the case of the moderate Pr fluid (see Fig.28). The amplitude of surface vibration is 4×10^{-4}, this value is equivalent to $1\mu m$ (see Fig.29).

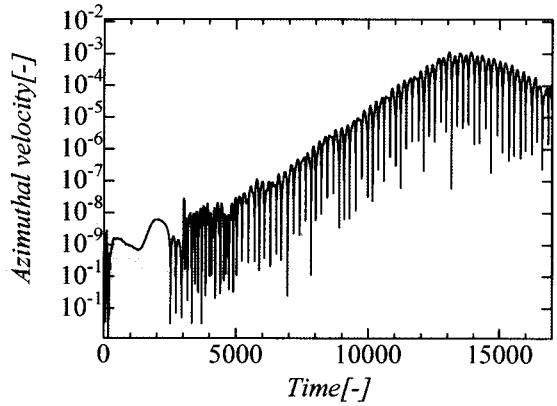

Figure 28: Absolute azimuthal velocity variation at z = 1/2H (Ma = 50000, Pr = 28, g = 1g)

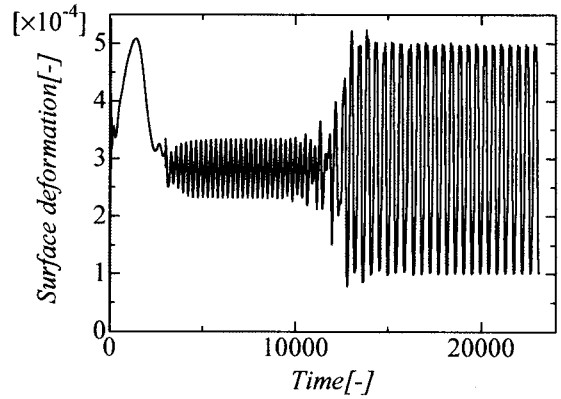

Figure 29: Dynamic free surface deformation in the pulsating flow state at z = 1/2H (Ma = 50000, Pr = 28, g = 1g)

5 CONCLUSIONS

The following conclusions were obtained from the present numerical studies.

(1) The thermocapillary convection with dynamic free surface deformation was calculated robustly and successfully.

(2) The result of the static shape of the liquid bridge gave good agreement with experiment.

(3) The results of the present was in good agreement with the results of linear stability analysis with respect to the critical Reynolds number.

(4) Effect of surface deformation upon the critical condition was found to be not significant in this case.

(5) The relation between the free surface deformation and the other quantities was explained.

(6) The phase lag between the temperature and the free surface deformation was observed in the oscillatory flow state.

(7) The free surface deformation was governed by the temperature difference in the axial direction at the upper part. As for the lower part, the temperature difference in the azimuthal direction dominates it.

(8) In the case of dynamic surface deformation the surface velocity is decreased and the surface temperature remained higher owing to the reduced vortex size.

(9) S-parameter was inapplicable to the moderate Pr number fluid. The position where the free surface is deformed most differed from that of the maximum surface velocity.

(10) Thermocapillary flow with high Pr number fluid was calculated successfully, and the pulsating flow was observed.

6 REFERENCES

[1] Kenning, D. B. R. 1968 Two-phase flow with nonuniform surface tension. Appl. Mech. Rev. 21, 1101-1111.

[2] Preisser, F., Schwabe, D. and Scharmann, A. 1983 Steady and oscillatory thermocapillary convection in liquid bridge columns with free cylindrical surface. J. Fluid Mech. 126, 545-567

[3] Velten, R., Schwabe, D. and Scharmann, A. 1991 The periodic instability of thermocapillary convection in cylindrical liquid bridges. Phys. Fluids A3 (2), 267-279

[4] Kuhlmann, H. C. and Rath, H. J. 1993 Hydrodynamic instabilities in cylindrical thermocapillary liquid bridges. J. Fluid Mech. 247, 247-274

[5] Savino, R. and Monti, R. 1996 Oscillatory Marangoni convection in cylindrical liquid bridges. Phys. Fluids 8, 2906-2922

[6] Shevtsova, V. M. and Legros, J. C. 1998 Oscillatory convective motion in deformed liquid bridges. Phys. Fluids 10, 1621-1634

[7] Kamotani, Y., Ostrach, S. and Masud, J. 2000 Microgravity experiments and analysis of oscillatory thermocapillary flows in cylindrical containers. J. Fluid Mech. 410, 211-233

[8] Kuhlmann, H. C. 1999 Thermocapillary Convection in Models of Crystal Growth. pp.11-18, Springer

[9] Goto, M., Shida, K., Ueno, I. and Kawamura, H. 2001 Numerical Simulation of Marangoni Convection in Consideration of Free Surface Displacement (Part 4). Marangoni Convection Modeling Research Annual Report

[10] Lappa, M., Savino, R. and Monti, R. 2001 Three-dimensional numerical simulation of Marangoni instabilities in liquid bridges: influence of geometrical aspect ratio. International Journal for Numerical Methods in Fluids. 36, 53-90

[11] Leypoldt, J., Kuhlmann, H. C. and Rath, H. J. 2000 Three-dimensional numerical simulation of thermocapillary flows in cylindrical liquid bridges. J. Fluid Mech. 414, 285-314

[12] Kawamura, H., Ueno, I. and Ishikawa, T. Study of Thermocapillary Flow in a Liquid Bridge towards an On-Orbit Experiment aboard the International Space Station. Advances in Space Research, accepted to appear

[13] Nishino, K. Private Communication (2001)

[14] Kuhlmann, H. C. Private Communication (2000)

[15] Kawaji, Private Communication (2001)

[16] Kuhlmann, H. C. and Nienhüser, Ch. Dynamic free-surface deformations in thermocapillary liquid bridge. submitted

[17] Kamotani, Y. and Ostrach, S. 1998 Theoretical analysis of thermocapillary flow in cylindrical columns of high prandtl number fluids. ASME Journal of Heat Transfer 120, 758-764